*Chapter 5*

# BREAKING FREE: EXTENDING THE ALUMINUM OXYNITRIDE EXPERIMENTS WITH TESSELLATED DATA

Sections of this chapter will be published in a forthcoming publication: **Gorske, S.F.**, Bhattacharya, K., Voorhees, P., Faber, K.T. "Grain ensemble effects on brittle crack propagation using Voronoi-Laguerre tessellations verified against real microstructures." In preparation.

## 5.1 Introduction

In the DCDC AlON samples of Chapter 4, neither the grain orientations nor the grain-averaged stresses are sure indicators of whether a crack will pass transgranularly through the grain or bypass it intergranularly. However, these parameters still have an impact on the sample's fracture toughness, and as seen in the two samples examined in the previous chapter, that value can change within and between samples as the grain configuration changes (Figure 4.11). As fracture toughness is calculated partly with the length of a crack, the grains just ahead of a crack after its motion has been arrested are a primary factor in obtaining that value. Determining how the grains in the volume ahead of the crack differ from those which the grain passed through unhindered should reveal more information on how the arrangement of grains of different sizes and orientations impacts the stress and strain states in those volumes, as well as the energy needed for the crack to progress through that region.

However, obtaining NF-HEDM maps of grain volumes and boundaries throughout an entire sample is not feasible. In the setup used for the AlON samples at Beamline 1-ID at the APS, a single NF-HEDM scan takes around 18 minutes, and the step size between scans was 5 μm. In contrast, one FF-HEDM scan takes around 7 minutes, and the beam size was 100 μm. In order to collect data at multiple stages of fracture, a balance must be struck between the number of scans performed and the time data collection takes. As a result, NF-HEDM data does not cover the entirety of most regions of interest, and the grain structure cannot be exactly determined everywhere.

Fortunately, FF-HEDM data contains some of the same information as NF-HEDM, primarily grain orientation, center-of-mass, and approximate spherical radius. In many

experiments, NF-HEDM is not performed at all, and tessellations are created using FF-HEDM to be used as approximate grain maps [1–4]. When examining suites of grains for average volumetric properties, this can often be a sufficient and efficient experimental design.

When considering transgranular versus intergranular fracture, as well as the question of which grains and grain boundaries arrested a crack's motion, however, the location of those grain boundaries must be accounted for. As such, using a tessellation as a grain map requires a more robust and experimentally-verified method to recreate the grain structure. The first part of this chapter will be concerned with testing various FF-HEDM tessellation creation methods against NF-HEDM ground truth maps, both from the AlON samples described in Chapter 4. Following the selection of one method, the second part of the chapter will examine what the tessellations reveal about the crack's interaction with AlON grains beyond the results of the previous chapter.

## 5.2 Methods: Creating and verifying HEDM tessellations

### *5.2.1 Mathematical basis: Voronoi and Laguerre-Voronoi tessellations*

The simplest form of tessellation is a Voronoi tessellation, requiring only a set of points to be used as centroids for the tessellated structure within the region of interest. The tessellation is formally defined in Equation 5.1 [5].

$$\widehat{V_i} = \{\boldsymbol{x} \in W \mid |\boldsymbol{x} - \boldsymbol{z_i}| \leq |\boldsymbol{x} - \boldsymbol{z_j}| \text{ for } j = 1, \dots, k, j \neq i\} \quad \text{Equation 5.1}$$

$\{\boldsymbol{z_i}\}_{i=1}^{k}$ = centroids $W$ = discrete set of points in volume of interest

Essentially, the tessellation can be created by assigning each discrete point in the volume of interest to the set for which the centroid is closer to that point than any other set's centroid. When the given centroids are well-dispersed in the volume, and when the sets (or grains, in this case) are known to have similar volumes, this approximation can work well to define the division of the larger volume into grains; however, it is limited when greater variability and irregularity is present in the grains' sizes and shapes [2,6]. Accordingly, a Laguerre-Voronoi tessellation can be defined (Equation 5.2), which minimizes a value known as the power-distance, $d_L$ (Equation 5.3) instead of $|\boldsymbol{x} - \boldsymbol{z_j}|$ [2]. By introducing a weight which decreases the power-distance more for larger values of the weight, the size of the set assigned to grains

with larger weights is thereby larger, making the power-distance an effective proxy for grain size. The weight in the power-distance is sometimes interpreted as being related to the square of the radius of the set [2].

$$\widehat{V}_i = \{\boldsymbol{x} \in W \mid d_L(\boldsymbol{x}, \boldsymbol{z_i}, w_i) \leq d_L(\boldsymbol{x}, \boldsymbol{z_j}, w_j) \text{ for } j = 1, \ldots, k, j \neq i\} \quad \text{Equation 5.2}$$

$$d_L(\boldsymbol{x}, \boldsymbol{z_i}, w_i) = |\boldsymbol{x} - \boldsymbol{z_i}|^2 - w_i \quad \text{Equation 5.3}$$

### *5.2.2 Using FF-HEDM data in the Laguerre-Voronoi tessellation*

The FF-HEDM data provides for every grain in the interrogated volume both the centers-of-mass and radii (calculated for a sphere of equivalent volume to the grain volume illuminated by the X-ray beam). When both NF-HEDM and FF-HEDM datasets exist for a given volume, a tessellation using the FF-HEDM information can be registered against the NF-HEDM grain map to determine its accuracy. In the AlON Sample 1, described in Chapter 4, three coincident NF-HEDM and FF-HEDM datasets (Table 5.1) were collected and used to optimize the tessellation methods described in the following sections. Two metrics were used to examine the tessellations: the first was the number of total points assigned to the same grain between the tessellation and the ground truth, while the second was the number of points with a NF-HEDM confidence value greater than 80% which matched between the two datasets. This second metric was used because near grain boundaries, the confidence level drops, and the observed boundary is much less clean than an actual grain boundary in AlON, which is expected to be near-planar. Thus, the percentage of matching points is expected to be low in those regions where the assigned grain may not be correct anyway, which could skew results. Figure 5.1a shows a sample NF-HEDM grain map, with the points with 80% or greater confidence shown in Figure 5.1b, showing much clearer grain shapes but without clear grain boundaries.

Table 5.1: Description of the FF-HEDM and NF-HEDM volumes used for tessellation optimization.

| | Load (N) | FF-HEDM volume | NF-HEDM volume | Percentage of points with >80% confidence |
|---|---|---|---|---|
| **Volume 1** | -1100 | A×300 μm | A×250 μm | 65.73% |
| **Volume 2** | -1700 | A×500 μm | A×300 μm | 54.72% |
| **Volume 3** | -1740 | A×700 μm | A×105 μm | 68.17% |

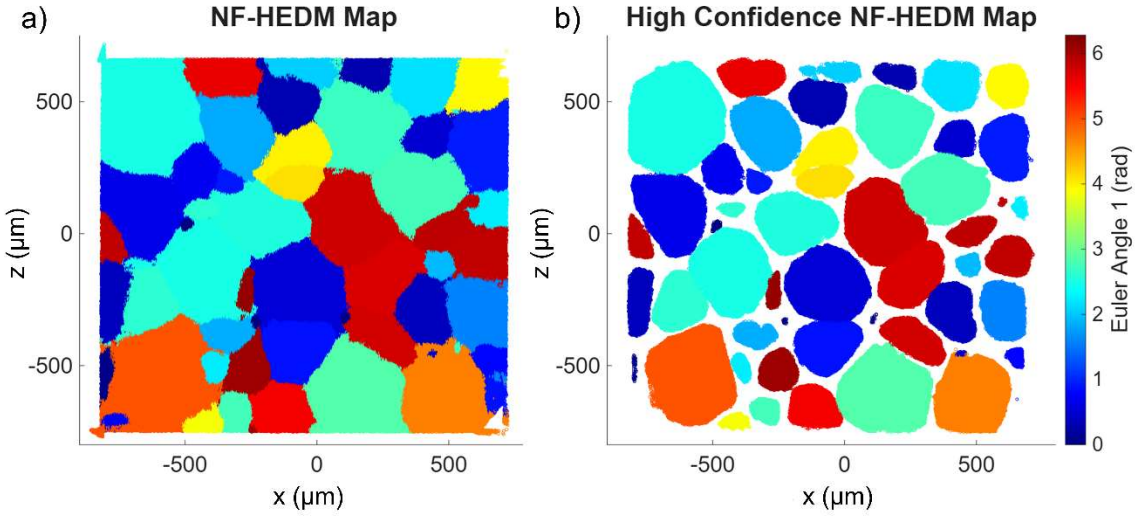


Figure 5.1: a) Near-field HEDM grain map from Volume 2 in Sample 1, colored by the first Euler angle. b) The map in a) with only points having a confidence value of 80% included, showing grain shapes without uncertain grain boundaries.

By substituting the centers-of-mass for the centroids in Equation 5.1, the basic Voronoi tessellation can be created. For the Laguerre-Voronoi tessellation, the spherical radius can then be used in creating the weight in the equation for the power-distance, but $w_i$ does not necessarily have to equal $r_i^2$, and may have additional factors determining its value.

Two different versions of the power-distance were tested as a first step. Equation 5.4 is similar to Equation 5.3, with the square of the radius having an additional weight factor that was probed at multiple values. Equation 5.5, meanwhile uses the square root of both the $|\boldsymbol{x} - \boldsymbol{z_j}|^2$ term and the $r_i^2$ term, while also weighting the radius to various extents.

$$d_L(\boldsymbol{x}, \boldsymbol{z_i}, w_i) = |\boldsymbol{x} - \boldsymbol{z_i}|^2 - b \cdot r_i^2 \qquad \text{Equation 5.4}$$

$$d_L(\boldsymbol{x}, \boldsymbol{z_i}, w_i) = |\boldsymbol{x} - \boldsymbol{z_i}| - b \cdot r_i \qquad \text{Equation 5.5}$$

The results for how well the tessellations matched the NF-HEDM ground truth are shown in Figure 5.2, indicating that for all the studied volumes, Equation 5.5 reached a greater maximum match percentage, achieved when the radius weight b had a value of around 1.25. The maximum values are reported in Table

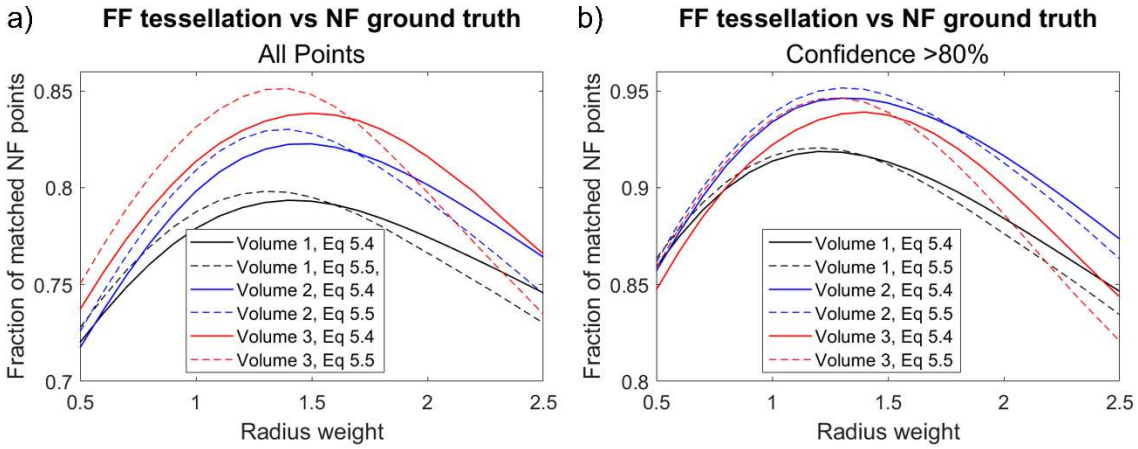


Figure 5.2: Results from Equations 5.4 and 5.5. a) Fraction of points attributed to the same grain as the equivalent NF-HEDM point, as a function of radius weight b. b) Fraction of correctly identified points using only NF-HEDM points with confidence >80%.

Table 5.2: Maximum percentage of ground truth NF-HEDM grain IDs matched by FF-HEDM tessellations using Equation 5.5.

| | **radius weight *b*** | **Percentage of matched NF points** | **Percentage of matched NF points in confident regions** |
|---|---|---|---|
| **Volume 1** | 1.2 | 79.68% | 92.06% |
| **Volume 2** | 1.3 | 83.01% | 95.15% |
| **Volume 3** | 1.3 | 85.11% | 94.64% |

### *5.2.3 Adjusting for orientation effects*

While adjusting the power-distance based on grain radius allows size effects to be included, the value of the power-distance for a given grain is constant at all equivalent distances from the grain centroid, and grains are not entirely spherical. While a tessellation does introduce planar boundaries between grains reminiscent of real grain boundaries,

impingement is not the only factor in determining where those grain boundaries will lie for most materials. Just as different planar arrangements of grains diffract at different angles, so too do those arrangements, with their unique spacings between sets of atoms, have different surface energies due to the atomic densities on the free surface [7]. As noted in Chapter 2, surface energy plays an important role in fracture, including the planes on which fracture is more energetically favorable. It also influences grain growth, as surfaces with lower surface energy can grow to larger areas when there are no other restrictions on where a grain can grow; minimizing the entire surface of a free grain results in a polyhedron with faces corresponding to the lowest surface-energy plane in that orientation.

While the surface energies of different planes for many elements and simple materials have been estimated, calculated, and tested [8], AlON does not have the same type of available data. For metals with the same face-centered cubic (FCC) structure as AlON, various analyses have been performed which have concluded that the {111} planes have the lowest energy of any surface, followed by the {100} plane, and thus these two plane families dominate the resultant grain shape (Figure 5.3) [7,9,10]. Thus, in the <111> directions, those grains might grow larger than the average radius of the grain, while in other directions the radius might be smaller.

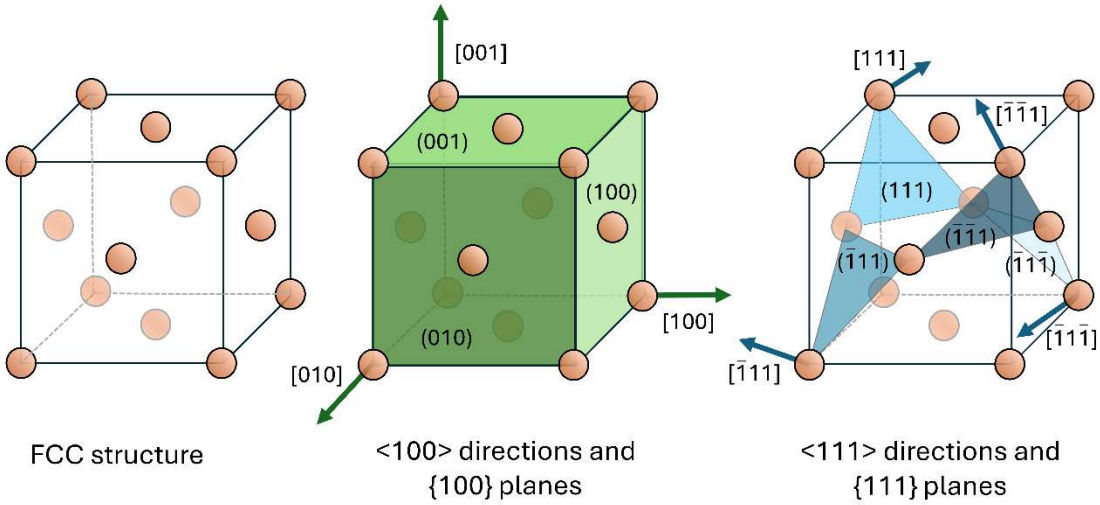


Figure 5.3: The face-centered cubic (FCC) structure, with the <100> and <111> directions and {100} and {111} planes pictured. For each set of directions and planes, the negative is also part of the same family but is not pictured for clarity.

To incorporate this aspect of real grains into the tessellation and the power-distance, the direction and distance of each point to each centroid in the tessellation was converted into a series of vectors. The orientation of that vector with respect to each grain's unit cell was then determined, then it was compared to the <100> and <111> vectors and the angles between them computed (Equations 5.6-7). Then an additional weighting factor was added to the power-distance based on the angular proximity to the two extremes. Since the <100> family has six equivalent directions, and the <111> family has eight, the closest vectors from each family, that is, those with the smallest angle between them and the location vector, were used for this calculation (Equation 5.8), which was then substituted into Equation 5.5 in place of $w_i$.

$$\boldsymbol{v} = \boldsymbol{Q}^{\boldsymbol{T}}|\boldsymbol{x} - \boldsymbol{z_i}| \qquad \text{Equation 5.6}$$

$$\theta = \cos^{-1}\frac{\hat{\boldsymbol{e}} \cdot \boldsymbol{v}}{\|\hat{\boldsymbol{e}}\|\|\boldsymbol{v}\|} \qquad \text{Equation 5.7}$$

$$w_i = b \cdot r_i\left(\frac{\theta_{\langle 111\rangle}(1-p) + \theta_{\langle 100\rangle}(1+p)}{\theta_{\langle 111\rangle} + \theta_{\langle 100\rangle}}\right) \qquad \text{Equation 5.8}$$

$\hat{\boldsymbol{e}}$ = unit vector for direction in grain

$\boldsymbol{Q}^{\boldsymbol{T}}$ = rotation matrix (grain reference frame to sample reference frame)

$p$ = relative change in radius

(<100> or <111>)  $\theta$ = angle between vectors

A range of values for $b$ and $p$ were tested while substituting Equation 5.8 for $b \cdot r_i$ in Equation 5.5, with results shown in Figure 5.4. Negative values for p correspond to the <100> directions having a larger radius, as $\theta_{<100>}$ will be smaller than $\theta_{<111>}$ for directions closer to the <100> pole, while the <111> directions are weighted more heavily for positive values of $p$.

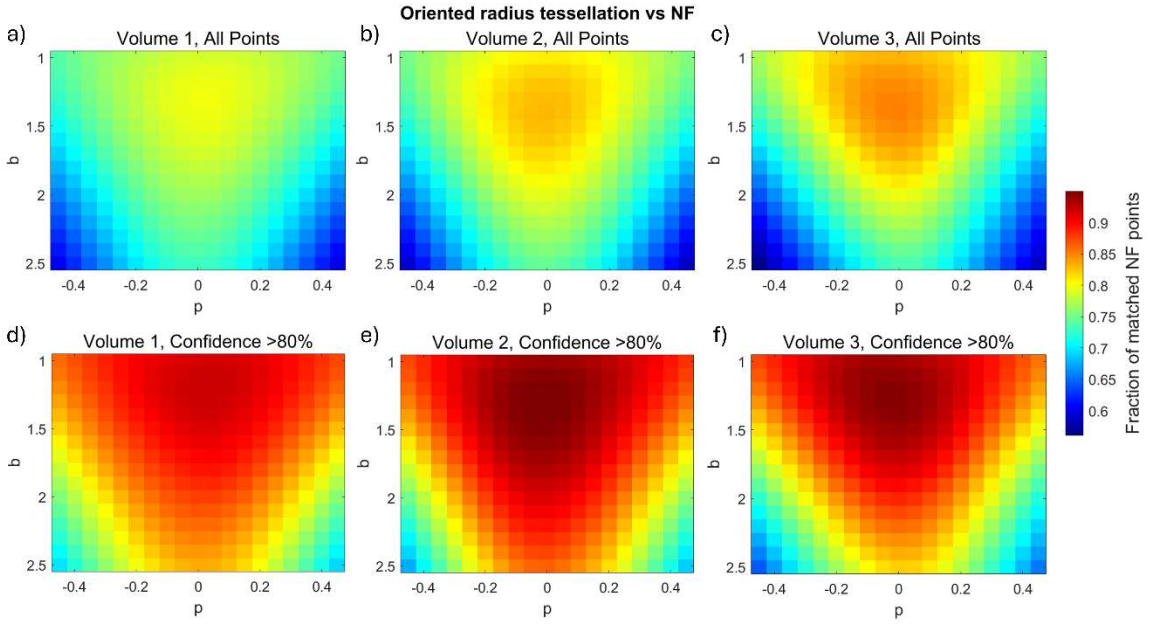


Figure 5.4: Results from using Equation 5.8 as the weighted factor in Equation 5.5.

As seen in Figure 5.4, the match between the tessellation and the NF-HEDM results for all volumes is maximized for some $b$ when $p = 0$. For $p = 0$, $w_i = b \cdot r_i$ and thus the result is unchanged from Equation 5.5 and the results tabulated in Table 5.2. Therefore, either the {100} and {111} faces have very similar surface energies in AlON, or any difference in directional growth for the grains is already accounted for by the distribution of the centroids in space.

### *5.2.4 Adjusting for volume effects*

One shortcoming of HEDM in tracking grains is that data is only reported for the illuminated volumes. Thus, the reported centers-of-mass are really the centers-of-mass for

the section of the grain in a specific volume, and the true centroids of grains which extend beyond the top and bottom layers of the scans will be more distant from the center of the interrogated volume than reported. This fact is likely why, in Figure 5.2 and Table 5.2, Volumes 2 and 3 have greater match percentages between the tessellations and NF-HEDM data; the FF-HEDM data for those scans extended beyond the edges of the NF-HEDM volume (Table 5.1), and so data from beyond the region of interest is used, including grain centroids from outside that volume. When creating tessellations for the entire volume of a set of FF-HEDM scans, however, this effect will be lost. Furthermore, because the radius reported by HEDM is calculated using only the illuminated volumes, grains on the edges of the volume will actually have larger radii than shown in the data. Additionally, grains on the edges of a sample can be artificially cut off as a result of processing, skewing their shape; the original grain's centroid and radius will also be shifted from the HEDM values.

Adjusting the centroids presents the issue that the direction between the true and reported values is unknown; perturbing it at random in its three directions of freedom might bring the tessellation closer to the actual grain structure, but doing so might also worsen the match. As such, it will not be adjusted in the method presented here. The radius, however, can be more easily perturbed, since as a scalar it has a single degree of freedom and the direction of perturbation should be an increase for those grains missing parts of their volume.

Checking the tessellation from Equation 5.5 for any grains which lie on the edge in order to adjust their radii is unnecessarily time-consuming, as it would potentially result in an iterative process as tessellated grains are moved toward and away from the boundaries of the illuminated volume. Accordingly, the weighted radii used in Equation 5.5 can simply be adjusted based on the distance of each grain's centroid to the center of the overall volume (Equation 5.9).

$$b_i = s \cdot \frac{d_i}{d_{max}} + b_0 \qquad \text{Equation 5.9}$$

$s$ = span between largest and smallest $b_i$

$d_i$ = distance of centroid $i$ to illuminated volume center

$b_0$ = smallest $b_i$

$d_{max}$ = distance of sample corner to illuminated volume center

Adjusting the span of weights $s$ that can be assigned to the power-distance and the minimum weight $b_0$ provides many opportunities for tailoring the tessellation. Since the match between the NF-HEDM maps and the tessellation from Equation 5.5 was maximized in the range of $b$ = 1.2-1.3, including that value in the range $b_i$ can take is sensible. A variety of spans ranging from 0 to 1 were tested, and both the overall match percentage and the percentage in the confident regions were increased for all volumes (Figure 5.5, Table 5.3) when $s$ was set to 0.25 and $b_0$ was set to 1.25, meaning that the range of values $b_i$ can take goes from 1.25 for a centroid at the center of the illuminated volume to 1.5 at a sample corner.

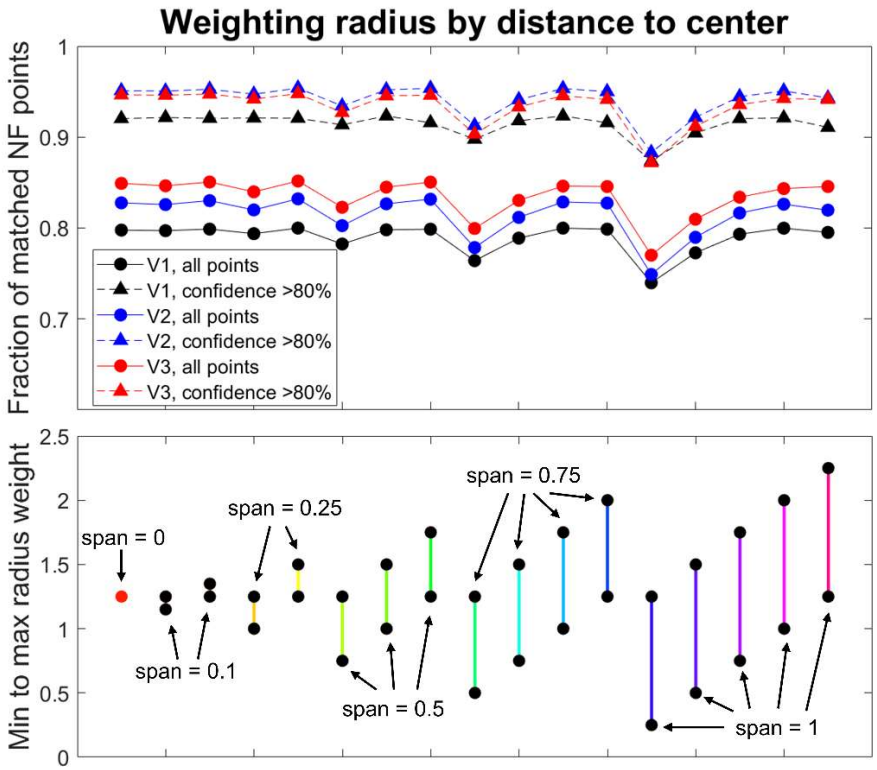


Figure 5.5: Results when the tessellation of Equation 5.5 is modified by Equation 5.9 so that the weight $b_i$ on the radius $r_i$ in the modified power-distance is determined by the distance of the centroid $z_i$ to the center of the illuminated volume. At the center of the volume, $b_i$ equals the minimum value of the range, shown in the bottom half of the figure, and it equals the maximum at the sample corner. The results for the verification of the tessellation against the ground truth NF-HEDM scans are reported at the top.

Table 5.3: The percentage match between the NF-HEDM grain maps and the FF-HEDM tessellation created by Equations 5.5 and 5.9, along with the increase in match percentage from the unmodified Equation 5.5. For Equation 5.9, $s = 0.25$ and $b_0 = 1.25$.

| | **Percentage of matched NF points** | **Increase in percentage matched from Table 5.2** | **Percentage of matched NF points in confident regions** | **Increase in confident percentage matched vs Table 5.2** |
|---|---|---|---|---|
| **Volume 1** | 79.99% | 0.22% | 92.07% | 0.04% |
| **Volume 2** | 83.21% | 0.44% | 95.39% | 0.29% |
| **Volume 3** | 85.17% | 0.26% | 94.77% | 0.13% |

While the increase in match percentage is modest, the fact that the increase was present among all tested volumes despite their different sizes demonstrates potential for this approach.

### *5.2.5 Using sub-granular FF-HEDM data*

In the AlON experiments, the FF-HEDM scans were taken 100 μm apart. However, many of the grains were larger in diameter than that distance, meaning they spanned two or more FF-HEDM layers, and values for the centroid, radius, and stress tensor were calculated for each local volume. Using this sub-granular data is therefore considered here as an alternative way to formulate the tessellations, which might allow non-spherical and asymmetrically shaped grains to be better matched in space.

First, the centroids for each sub-granular volume were assumed to lie along a linear path (Figure 5.6a). Calculating a first-order line of best fit is trivial, and equations were created to track $x$ and $z$ as functions of $y$, the direction in which the sample was moved to take subsequent scans. Thus, the tessellation can be divided into any number of 2D slices in the $y$ direction and a centroid for that slice can be calculated (Figure 5.6b).

Similarly, an equation for the radius as a function of $y$ was created. It is assumed that the grain's volume, and consequently the reported radius, is maximized in its center (Figure 5.6a). In order for the equation to reach a single maximum, and for it to remain concave everywhere, a parabolic fit is used (Figure 5.6b). Since most of the AlON grains have radii smaller than 200 μm, very few should appear in more than three FF-HEDM scan volumes, so a fit of greater power is prohibited anyway.

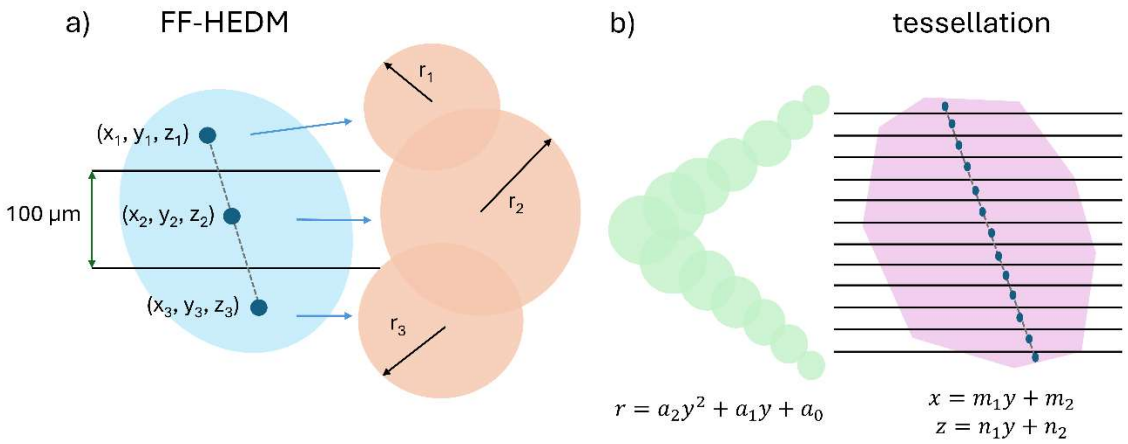


Figure 5.6: Using sub-granular FF-HEDM information to construct a series of 2D tessellations. a) Each FF-HEDM scan reports a center-of-mass and radius for each scan volume. b) By creating equations for $x$, $z$, and $r$ in $y$, arbitrarily many 2D slices can be made in the volume, each with a value for $x$, $z$, and $r$.

For grains in only two volumes, two possible cases exist: first, that the grain is cut off by the edge of the FF-HEDM volume, and second, that it is fully contained within the volume. To determine which case each grain fell into, the conditions in Table 5.4 were used. If all conditions were satisfied, the grain was guessed to have part of its volume lying outside the FF-HEDM volume.

Table 5.4: Conditions for determining if part of a grain's volume lies outside the scanned FF-HEDM volume.

| Condition | Reasoning |
|---|---|
| One sub-granular volume must be present in top or bottom FF-HEDM scan. | The grain must be on the edge of the FF-HEDM volume. |
| The sub-granular radius from the edge scan must be bigger than that from the inner scan. | If the grain radius is decreasing, the centroid is within the FF-HEDM volume already. |
| Both sub-granular radii must be greater than the scan height (100 µm). | The cumulative volumetric radius indicates a diameter greater than the height of two scans. |

The grains with one or two FF-HEDM presences then had to have additional center-of-mass and radius values manufactured in order for the fits to be created, according to Figure 5.7 and Table 5.5. Two-datapoint grains determined to be interior to the FF-HEDM volume

were assigned a point midway between the two existing *y* values with a radius calculated from the combined spherical volume of the existing datapoints. For the edge grains, since it cannot be determined how much grain volume might lie outside the FF-HEDM volume, and since most grains are not present across more than three sub-volumes, only one external value was added to those grains with two datapoints, and was equal to the smaller radius at a *y*-position mirrored across the *y*-position closer to the volume edge. Grains present in a single sub-volume could not be determined as having additional volume outside the scanned volume, and were assigned additional radius and *y* values corresponding to a sphere centered at the existing datapoint. The *x* and *z* positions for the linear fit were made to be constant and independent of *y*.

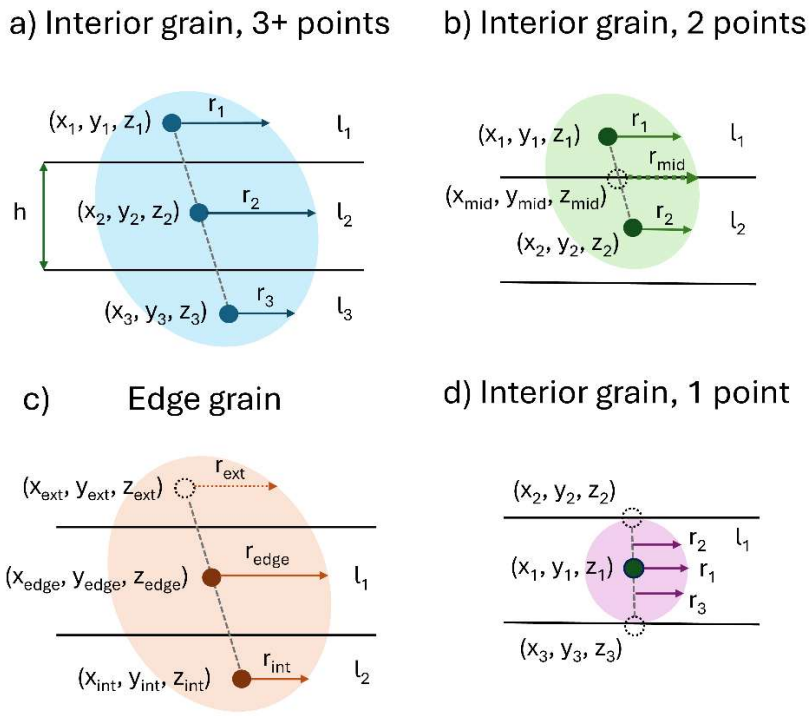


Figure 5.7: Possibilities for how grains present in FF-HEDM, and how the 2D-slice tessellations described in Table 5.4 can be created for each.

Table 5.5: Criteria and calculations for adding additional points to FF-HEDM grains in order to calculate polynomial fits.

| Criterion | Radius Equation | $y$ Equation |
|---|---|---|
| 2 points, fully within FF-HEDM volume | $r_{mid} = \sqrt[3]{r_1^3 + r_2^3}$ | $y_{mid} = \frac{y_1 + y_2}{2}$ |
| 2 points, grain bisected by edge | $r_{ext} = r_{int}$ | $y_{ext} = 2y_{edge} - y_{int}$ |
| 1 point | $r_2 = r_3 = \frac{\sqrt{3}}{2} r_1$ | $y_2 = y_1 - \frac{r_1}{2}$<br>$y_3 = y_1 + \frac{r_1}{2}$ |

Once the radius, and center-of-mass for every grain could be calculated based on $y$-position, tessellations could be made according to Equation 5.5, but with a separate calculation for each $y$-position of interest. Additionally, if the radius for a certain grain in a certain 2D slice would be negative, its value was set to zero and the center-of-mass for that grain was placed far outside the region of interest, so it would not be at risk of minimizing the power-distance. Results are shown in Figure 5.8. contrasted against the results from using Equation 5.5 and Figure 5.2 in its 3D form, the latter of which is shown to perform better both for the set of all NF-HEDM points and the set of confident points.

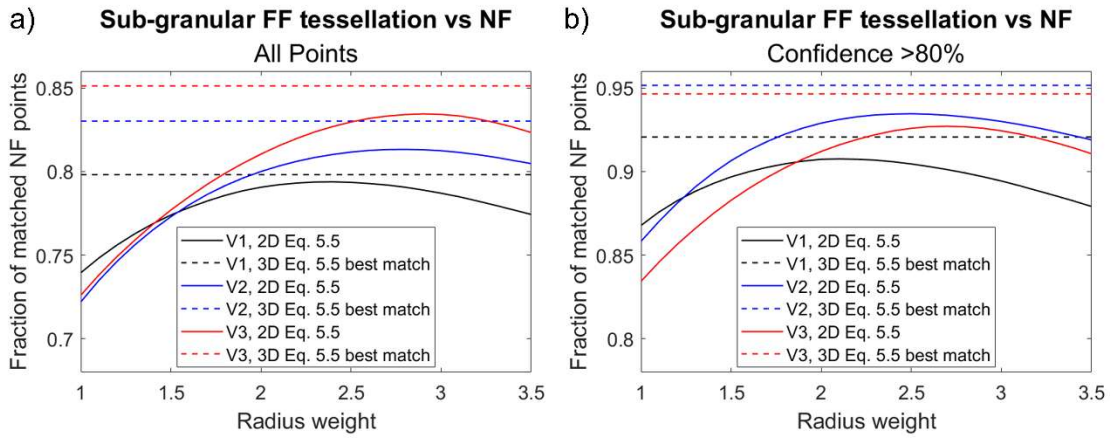


Figure 5.8: Results from making 2D-slice tessellations using Equation 5.5 and sub-granular FF-HEDM data as presented in Figure 5.6-7 and Tables 5.4-5. The best results for each volume from the 3D tessellation using Equation 5.5 are also shown for comparison, and show that the 3D tessellation is a better match for all volumes and confidence levels.

### *5.2.6 Correcting for volume mismatches*

An additional piece of information that can be obtained from FF-HEDM and used independently of NF-HEDM is the overall grain volume. Exact volume matches are not generally possible, since the FF-HEDM volumes, and therefore the sub-granular volumes, usually do not exactly overlap with the NF-HEDM volumes, as seen in Table 5.1. However, the relative volume of a grain within the FF-HEDM volume can be compared to its relative volume in the tessellation (Equation 5.10).

$$\Delta V_i = \frac{V_{i,ff}}{\sum_{j=0}^{n} V_{j,ff}} - \frac{V_{i,tess}}{\sum_{j=0}^{n} V_{j,tess}} \qquad \text{Equation 5.10}$$

An iterative procedure was performed using this information. The grain boundaries in the tessellation along the $x$, $y$, or $z$ direction were found, and the $\Delta V$'s of the grains on either side compared. If both had the same sign, then nothing was done. If they had opposite signs, this indicated that one tessellated grain was smaller than its FF-HEDM counterpart (positive $\Delta V$), while one was larger (negative $\Delta V$). The boundary was then changed by one voxel for every point along the boundary, increasing the too-small grain's volume and decreasing the larger grain's volume. The procedure was repeated for the other two orthogonal directions. All three directions could then be iterated over an arbitrary number of times until the average of the $\Delta V$'s neared zero.

Results are shown in Figure 5.9. While the match for Volume 1 increases very slightly with two iterations, overall it does not change very much, while the matches for Volumes 2 and 3 become increasingly worse. This is likely because of the difference in size between the FF-HEDM and NF-HEDM volumes (Table 5.1); while the sizes are similar for Volume 1, meaning that the relative grain sizes are roughly accurate, the data for Volumes 2 and 3 extend beyond the borders of their respective NF-HEDM volumes, meaning that the relative grain volumes are quite different between the NF-HEDM-sized tessellations and FF-HEDM. As a result, iterating causes grains extending beyond the upper and lower bounds of the volume, which have a lesser contribution to the NF-HEDM volume than the FF-HEDM volume, to grow into regions where they should only have minimal presence. When creating a tessellation with no ground truth, extending the full volume of an FF-HEDM dataset, this error may be mitigated, but without an appropriate dataset for comparison, the conclusion is to use the original tessellation without attempting to correct the grain-volume mismatches.

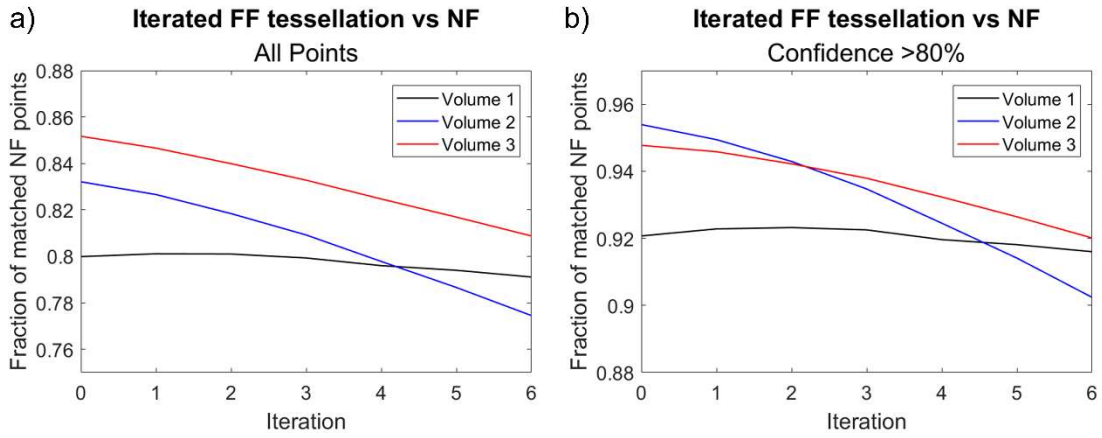


Figure 5.9: Results from iterating the tessellations made from Equation 5.5 to bring the relative tessellated grain volumes closer to the relative FF-HEDM grain volumes. Apart from a slight increase in the match fraction for Volume 1 after two iterations, this approach does not improve the tessellations' match to the NF-HEDM data.

### *5.2.7 Quantifying grain boundary accuracy*

Given that the NF-HEDM grain boundaries are uncertain, the question arises of how well a grain can be determined to have cracked trans- or intergranularly. Using a tessellation with an additional level of uncertainty near the boundaries further complicates grain assignation. Quantifying the uncertainty would allow for some restrictions to be placed on how close the crack can come to the tessellation boundary to be considered as potentially being intergranular for a particular grain.

First, the difference between the nominal grain boundary and its true location must be estimated. As seen in Figure 5.1a, the grain boundaries resulting from assigning each NF-HEDM point to the closest-match grain, even if that match has low confidence, are irregular and imprecise. Restricting the confidence to 80% (Figure 5.2b) leaves some gaps between grains, but in some regions that gap is negligible, with a clean grain boundary appearing. The true grain boundary should also be clean and approximately planar, and should therefore lie somewhere between the nominal and confident boundaries. Exactly how wide that gap tends to be must be determined as a first step for an uncertainty estimate.

Simply summing the volume of each individual voxel assigned to a grain in NF-HEDM and calculating the equivalent spherical radii is not the most ideal estimate for either the overall size of the grain or its confident volume, since, as previously explicated, many of

these grains may be cut off by the edges of the interrogated volume or the sample. Instead, the necessary information is the average difference between the surfaces of those volumes. By measuring the distance to the centroid from every point on both surfaces, the difference in those average distances can be measured. Additionally, there is then no need to eliminate datapoints from the volume surfaces, since the same distances would be calculated for both the confident and regular sets of voxels and will thus cancel out.

The same calculation can be performed on the voxels assigned to a grain from the tessellation to determine how far the tessellation's estimated boundary is from the approximate NF-HEDM one. The results from both calculations are presented in Table 5.6. Neither set of calculations trends with the overall FF-HEDM grain size.

Table 5.6: Differences between boundaries between the ground-truth NF-HEDM results and the best match tessellations.

| | **Δ(mean nominal NF boundary – mean confident NF boundary) (μm)** | **Δ(mean nominal NF boundary – mean tessellation boundary) (μm)** |
|---|---|---|
| **mean** | 20.95 | 4.79 |
| **median** | 20.00 | 4.26 |
| **standard deviation** | 9.29 | 13.01 |
| **extrema** | 55.79 | -39.31, 44.34 |

Promisingly, the average difference between the NF-HEDM results and the tessellations is near zero, indicating that the tessellation does not trend toward over- or under-sizing grains. In general, the difference between the nominal but uncertain NF-HEDM boundary and its confident volume is a few tens of microns, which is about the same value as two standard deviations in either direction from the mean for the NF-to-tessellation difference. Therefore, allowing for an uncertainty in the tessellation boundary of about 30 μm in either direction should account for most of the error in the tessellation and also likely capture the true grain boundary.

### *5.2.8 Choosing a tessellation*

As seen in Figures 5.4 and 5.8, attempts to use physical properties and sub-granular data, respectively, to correct the Laguerre-Voronoi tessellation, calculated by Equation 5.5 and

shown in Figure 5.2, were unsuccessful in increasing the percent match of the tessellation to the NF-HEDM ground truth. The adjustment of Equation 5.5 by Equation 5.9 with the correct parameters did provide a modest increase in percent match (Table 5.3, Figure 5.5), so that adjustment was carried into the creation of tessellations for regions without NF-HEDM data. Pictorial results for the final tessellation are shown in Figure 5.10, with comparison to the ground truth.

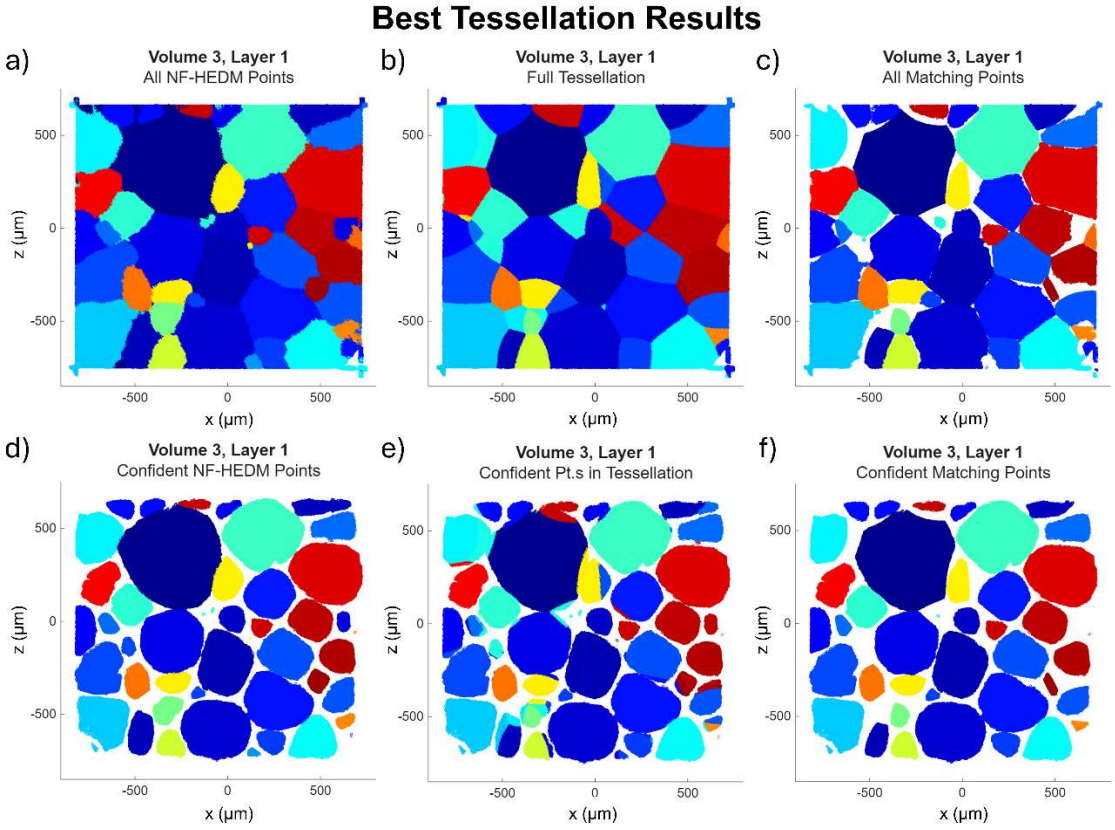


Figure 5.10: Results from the best tessellation, a combination of Equations 5.5 and 5.9, in a single 2D layer from Volume 3 in Sample 1. a) The full NF-HEDM reconstruction. b) The full tessellation. c) All points with the same grain assignation in both a) and b). d) The points in a) with confidence greater than or equal to 80%. e) The points from d) with their tessellated grain assignations. f) The points with the same grain assignation in both d) and e).

Tessellations were produced for regions in Sample 4 where FF-HEDM data was taken and the crack passed through, but for which no NF-HEDM data was available. Sample 1's FF-HEDM data without corresponding NF-HEDM were all taken in regions which did not crack and were thus not useful for determining crack behavior with regard to microstructure; additionally, the volume that was intersected by the crack was moved through completely in

one extension event, meaning that no grain boundaries were obtained for grains which arrested the crack. In contrast, the crack stopped within some of the FF-HEDM volumes in Sample 4. The tessellations were generated with 200 evenly spaced points in $x$, $y$, and $z$, for voxels with side lengths of 6-8 μm. The tessellation's extrema were defined as ±50 μm from the extrema in the spread of FF-HEDM centroids.

An additional point of interest for the FF-HEDM scans of Sample 4 is that 12-15 100 μm-tall scans were taken for every load state, compared to 3-7 in Sample 1. As a result, the volumes all share some overlap with the preceding state, and often some of the state prior to that as well. Thus, the tessellations from subsequent scans can be checked against each other to verify the method works properly to assemble grains, even without the NF-HEDM maps being available. A sample location present in three of the FF-HEDM volumes is shown in Figure 5.11. In general, the grains exist in the same location with approximately the same size and shape among all three tests. The grain boundaries, and therefore the trijunctions between grains, can vary by a few tens of microns, in accordance with the acceptable expectations for error in Table 5.6.

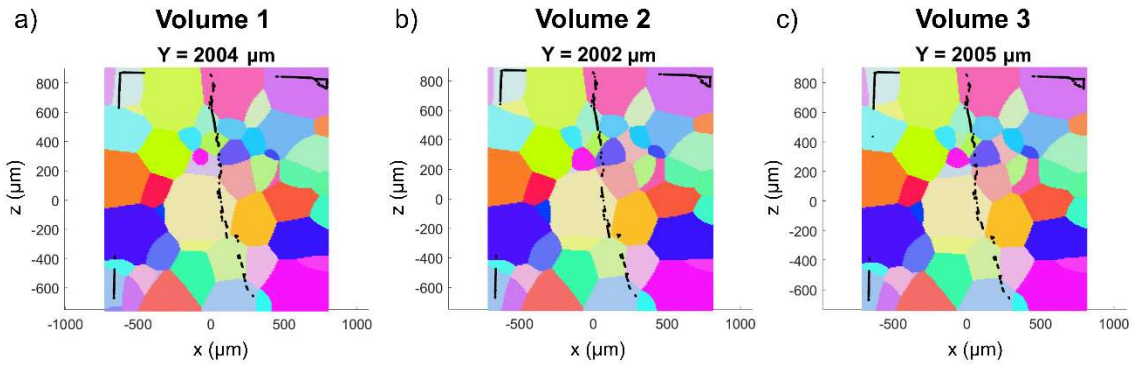


Figure 5.11: Tessellation sections from three FF-HEDM scans in Sample 4 with volume overlap. A representative 2D section is shown for each, demonstrating general similarity with some differences in grain boundaries and their distances to the crack. a) Volume 1, spanning 942 μm to 2451 μm. b) Volume 2, spanning 1536 μm to 2755 μm. c) Volume 3, spanning 1733 μm to 1961 μm.

### *5.2.9 Registering the tessellation to the crack*

Registering the tomographic crack data to the tessellation can be performed just as it was to the NF-HEDM data in Chapter 4. From the tessellation, each grain's centroid was recalculated, since in the Laguerre-Voronoi formulation, the tessellation and seed centroids may not be identical [2]. The maximum distance from that point to the grain's surface was also calculated; grains which had a nearby crack point within 120% of that distance from the centroid were retained for examination as having been potentially intersected. As there was some overlap between the FF-HEDM volumes and therefore the tessellation volumes, grains which appeared in multiple volumes were examined for average edge-to-crack distances. Grains were then sorted into categories as defined and described in Table 5.7; the ±30 μm estimate for grain boundary accuracy (Table 5.6) was used to identify grains which were not clearly intergranular or transgranular. Additionally, grains which likely arrested the crack were identified when the last local crack points existed solely above the crack, within 55 μm (the grain boundary uncertainty plus the crack depth uncertainty from Chapter 4). Multiple assignations could be given if different branches of the crack intersected the same grain or if a grain arrested the crack at first but it later passed through intergranularly or transgranularly.

Table 5.7: Categories and definitions for tessellated grains near to the crack.

| Category | Definition |
|---|---|
| Most likely transgranular | Crack cuts across grain; maximum distance to edge > 30 μm |
| Most likely intergranular | Crack parallel to and within 1 voxel of grain boundary |
| Uncertain | Crack passes within or outside grain by maximum 30 μm |
| Most likely arrested | All nearby crack points are above grain, within 55 μm |

## 5.3 Results

### *5.3.1 Grain orientations*

More than 1600 μm of the crack in Sample 4 was present in one or multiple tessellated volumes, resulting in many more grains identified as intergranular or transgranular than in the NF-HEDM results from Sample 1, although the percentages of each group compared to the total number of grains was similar (Table 5.8). With the additional information gained on grains that arrested the crack, orientation maps for the grains and the crack planes within them can be created to supplement Figure 4.10a,b (Figures 5.12-13). As before, in Figure 4.10c-f, the intergranularly- and transgranularly-cracked grains, and those which might belong to either group, do not display any prominent orientation preferences or persistent misorientations when compared to the other groups (Figures 5.12a-c, 5.13a-c). Furthermore, the grains which appear to have arrested the crack also have orientations and normals spread over the entirety of orientation space, both for those with a final arrested state and those which eventually propagated (Figures 5.12d-g, 5.13d-g).

Table 5.8: Numbers of total grains and those which cracked transgranularly or intergranularly in the studied volumes (one 250 μm-tall NF-HEDM volume for Sample 1 and a total of 2 mm of crack-containing tessellations for Sample 4).

| | Number of grains in Sample 1 NF-HEDM | Percentage of grains in Sample 1 NF-HEDM | Number of grains in Sample 4 tessellation | Percentage of grains in Sample 4 tessellation |
|---|---|---|---|---|
| Transgranular | 10 | 11.4% | 43 | 12.4% |
| Intergranular | 6 | 6.8% | 11 | 3.2% |
| Uncertain | — | — | 19 | 5.5% |
| Total | 88 | | 347 | |

Another piece of information not formerly available due to the small data size is orientation changes close to grain boundaries; the same 30 μm distance used to determine possible intergranular status was used to define “close”. Figure 5.13h shows the orientation planes that did crack for each grain and the changes between adjacent grains in blue, versus the potential grain-frame orientations that the crack apparently avoided by changing direction, in red. As there are no preferential orientations onto which the crack plane might be diverted, however, there is no apparent consistency between the orientation changes. Some changes lead the crack to reside on a very different plane while “avoiding” a plane with much smaller misorientation, while two grains with a similar crack plane might see that plane diverted to completely different orientations upon exiting. Thus, as noted in Chapter 4.4.1, crack direction and orientation must be more dependent on localized and volumetric effects than on individual grains’ properties, leading to gradual changes to the crack both before and after its interaction with a specific local volume.

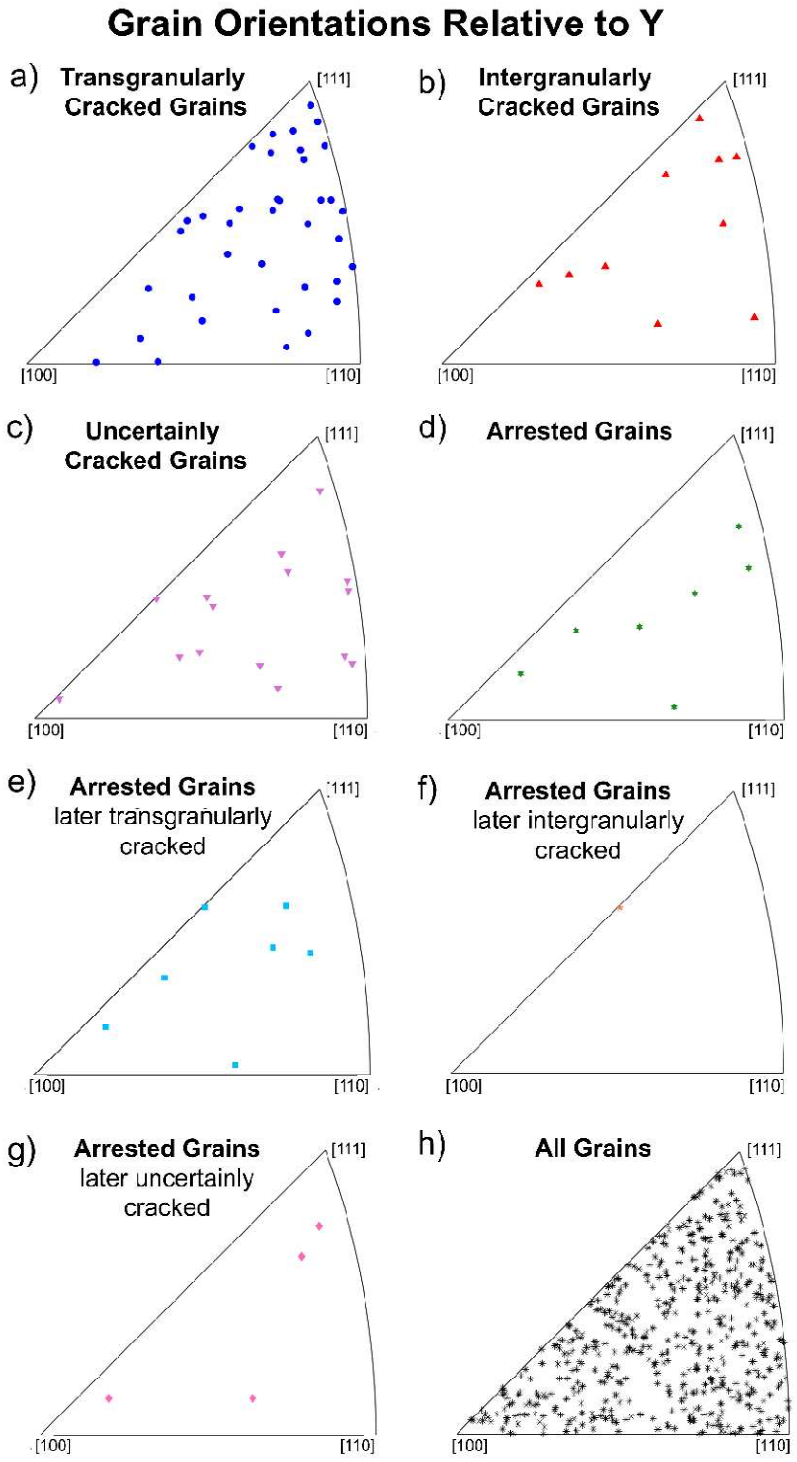


Figure 5.12: Inverse pole figures showing the orientations of FF-HEDM grains in Sample 4, relative to the loading ($y$) direction, identified as belonging to one or multiple groups described in Table 5.7. As in Figure 4.10, the groups do not display major distribution differences.

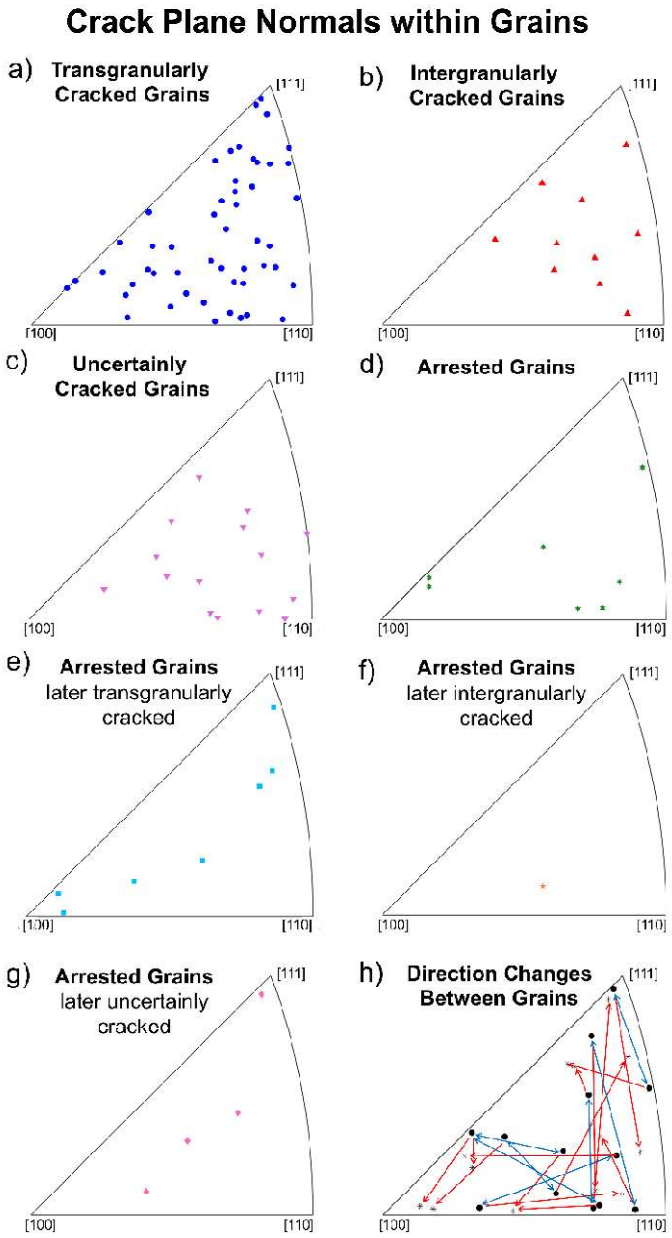


Figure 5.13: a-g) Distributions of the directions normal to the average crack plane in Sample 4 within each grain's unit lattice, with grains sorted into the groups described in Table 5.7, and generally distributed without trend. h) For cracks which changed direction near a grain boundary, the plane normal in both grains (dots), the crack orientation change between them (blue), the potential crack plane normal in the neighboring grain if the direction change did not occur (stars), and the crack orientation different to that normal (red), again without obvious trends.

While the overall orientation of the grains which appear to have arrested the crack in any capacity also do not follow a trend, by extracting the grain boundaries ahead of the crack, their normal vectors can be calculated and may reveal additional information. Figure 5.14 shows these vectors for the grains identified as arresting the crack and further delineates them into those which later cracked transgranularly, intergranularly, or uncertainly, and those which continued to arrest the crack until the end of the experiment. As noted in Chapter 4.4.3, sharp deflections of the crack, especially during a fast propagation event, are generally rare; thus, only a single grain later cracked intergranularly, and only because the original arrest occurred very close to that boundary. As expected, the grain which later cracked intergranularly has the smallest $y$ component and the largest-magnitude $x$ component due to the presence of the grain boundary on which it passed; the uncertain grains also have larger-magnitude $x$ components as the grain boundaries slope down near their edges where the crack moved through (Figure 5.14c). The grains which first arrested the crack and later passed transgranularly also generally have smaller $y$ components than the grains which were still arresting the crack at the end of the experiment, but larger $y$ components than the other two populations. Thus, the crack reached the final arresting grains at planes nearly perpendicular to its direction of motion, which provided an effective barrier to further extension. For the grains which were later cracked transgranularly, the crack either had to divert slightly, if possible, to a more favorable plane, or it reached the grain at those planes initially, making them easier to crack.

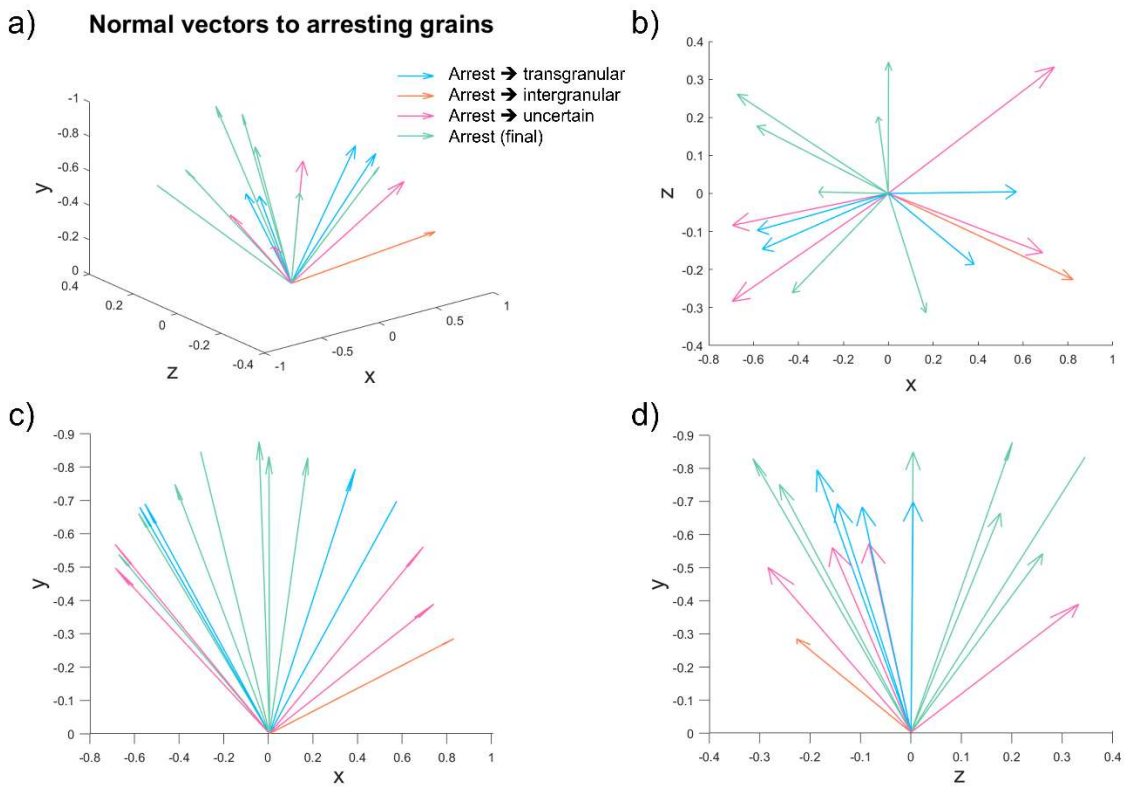


Figure 5.14: Grain boundary normal vectors ahead of the crack in Sample 4. a) 3D space b) $x$ and $z$ components c) $x$ and $y$ components d) $y$ and $z$ components. The grains which permanently arrested the crack have greater y components, indicating the crack reached them head-on.

### *5.3.2 Grain mechanical states*

Similarly to the orientation results, while the analysis of grain stress states in the NF-HEDM data of Sample 1 did not show any particular trends (Figure 4.10a-b), those results can be expanded upon with the addition of more grains, overlapping volumes, and information on grains and regions which arrested the crack from the Sample 4 tessellations. Figure 5.15 shows the results from three FF-HEDM volumes with different grains highlighted. Figure 5.15a), c), and e) depict the volumes with overlaid information for grains which have already interacted with the crack; that is, those that have already cracked intergranularly or transgranularly, or been arrested, while Figure 5.15b), d), and f) show those same volumes with overlaid information for grains which cracked or which arrested the crack in the following extension. Volume 1 overlapped with the crack front after the first extension, and thus includes grains of all types (Figure 5.15a); the next two extensions both added less

than 100 μm to the overall crack length, and so few additional grains were identified as interacting with the crack, although some did arrest it (Figure 5.15b). Volume 3, meanwhile, contained only a few grains which had already cracked prior to the data collection (Figure 5.15c), but the ~800 μm extension that occurred next resulted in acquiring information on the stress states of many grains before they were cracked or arrested the crack (Figure 5.15d). Finally, Volume 4 was taken after that extension and did include the crack front with data on arrested grains and a few others (Figure 5.15e); however, examining that volume for grains which had not yet interacted with the crack did not uncover any which cracked in the next extension (Figure 5.15f). The next extension was the final one, and as described in Chapter 4.3.2, this extension did not propagate from the original crack front, but represented a second crack front that branched off of the initial one before propagating through the entire sample volume (Figure 4.3e-f). Thus, the previous Volumes 1 and 3 were examined for information on grains which cracked or arrested the crack with the new extension (Figure 5.15g-h).

As reported in Chapter 4.3.3, the stress values for all populations display no obvious trends. Representative statistics are reported in Table 5.9, with stresses normalized to the overall sample load for comparison. In both the $x$ and $y$ directions, the stresses in grains already cracked or arrested before the FF-HEDM data collection fall within similar ranges for all populations. For data taken before the crack reached the grains of interest, both $\sigma_{xx}$ and $\sigma_{yy}$ for the grains about to arrest the crack are higher than for grains of other populations, but are still within one standard deviation of the other population means as well as the mean stress for all grains in the volume.

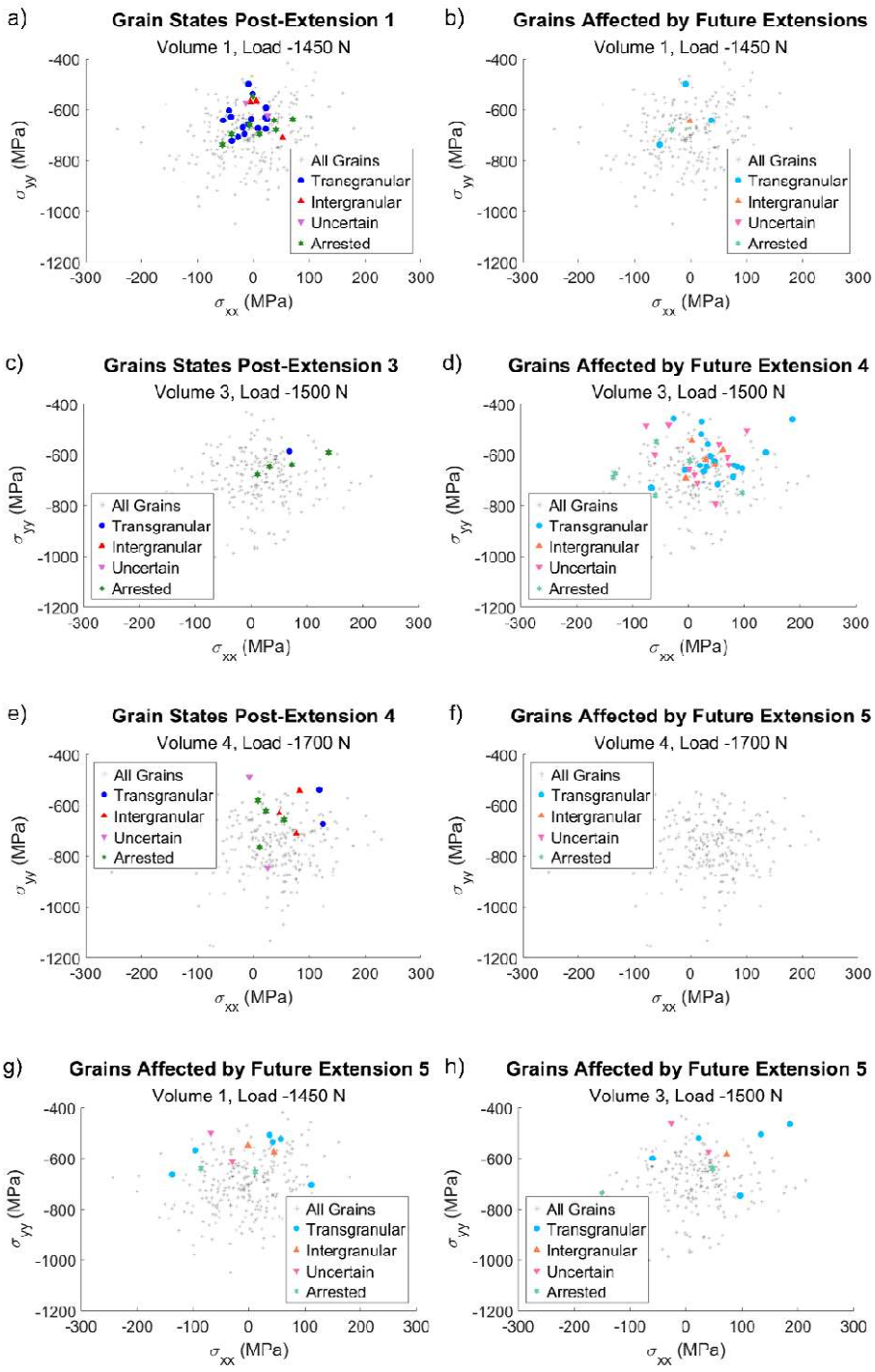


Figure 5.15: Stress states for FF-HEDM grains in Sample 4, highlighting those interacting with the crack. a,c,e) Highlighting grains which interacted with the crack before the FF-HEDM data was acquired. b,d,f-h) Highlighting grains which have not yet interacted with the crack.

Table 5.9: Stress statistics, calculated after normalizing to the overall load, for FF-HEDM grains in Sample 4, grouped into type of crack interaction and whether the FF-HEDM data is from before or after the interaction.

| | **Already interacted** $\sigma_{yy}/\sigma_a$ | **Not yet interacted** $\sigma_{yy}/\sigma_a$ | **Already interacted** $\sigma_{xx}/\sigma_a$ | **Not yet interacted** $\sigma_{xx}/\sigma_a$ |
|---|---|---|---|---|
| **Transgranular** | 0.95 ± 0.14 | 0.92 ± 0.13 | -0.020 ± 0.10 | -0.062 ± 0.084 |
| **Intergranular** | 0.90 ± 0.11 | 0.93 ± 0.09 | -0.059 ± 0.048 | -0.035 ± 0.041 |
| **Uncertain** | 0.87 ± 0.16 | 0.91 ± 0.15 | 0.011 ± 0.055 | -0.029 ± 0.086 |
| **Arrest** | 0.99 ± 0.10 | 1.02 ± 0.11 | -0.018 ± 0.091 | 0.066 ± 0.11 |
| **All grains** | 1.04 ± 0.16 | | -0.026 ± 0.095 | |

Due to the overlapping nature of the examined volumes, the changes in mechanical state for individual grains can also be explored. While the overlap was often small, only a few FF-HEDM scans or a few hundreds of microns, some grains of all the examined types had data from at least two scans (Figure 5.16). With so few data points, definitive claims will not be attempted, but in general, arresting grains, especially those which remained arrested for both scans in a comparison, tend to take on more tensile stress upon increase in load, with the magnitude of $\sigma_{xx}$ increasing and that of $\sigma_{yy}$ decreasing. This most likely is because without the barrier of the arresting grains, the crack would ideally open in that location, but due to the hindrance of its location and grain boundary orientation, a greater force is needed to do so when compared to more easily cracked grains. Meanwhile, grains which were cracked intergranularly or transgranularly in between the two scans have $\Delta\sigma_{xx}$ closer to, if not less than, zero, indicating a relief in stress as the crack is no longer being forced to open there.

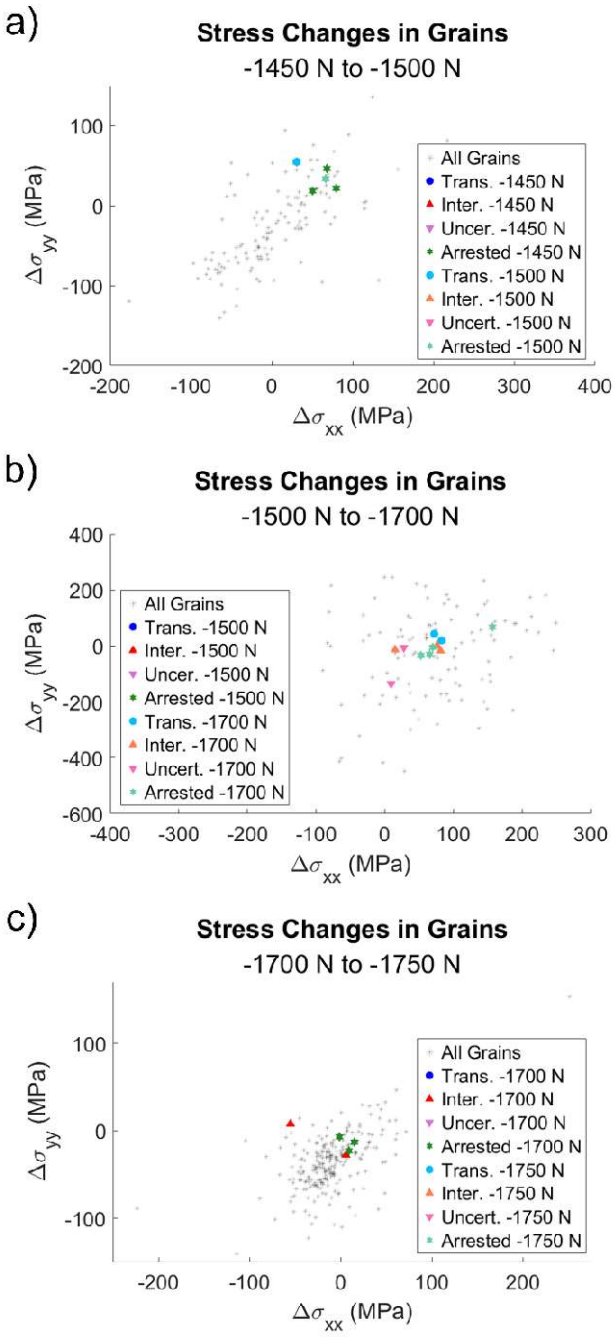


Figure 5.16: Changes in grain stress state between subsequent loading steps in Sample 4, with grains interacting with the crack highlighted similarly to Figure 5.17. Grains which had already cracked or arrested the crack by the time of the first scan are differentiated from those which were cracked or arrested the crack during the next extension, just before the second scan.

## 5.4 Discussion

### *5.4.1 Volumetric effects on crack extension*

Chapter 4 and the previous section demonstrate that while individual grain properties do affect the crack in measurable ways, the interaction of the grains with each other produces other emergent effects which are more difficult to relate to specific crack movements. For example, while the fracture toughness of individual AlON grains can be calculated [11], studying an entire suite of grains can only result in obtaining the average local fracture toughness. However, this is not to indicate that such properties are beyond understanding or disassembling.

The local stress environment is explored in Chapter 4.3.1 and Figure 4.7, and this analysis can be extended by considering the strain energy density of the material. Strain energy is a measure of how much internal energy is contained within a volume as a result of stress buildup, and the variance of that energy independent of volume is the strain energy density *W*, the grain-averaged value of which can be calculated using Equation 5.11 and the FF-HEDM strain and stress tensors [12]. The strain energy density is also related to the stress intensity factor and strain energy release rate in that it can be related to the total amount of internal resistance to crack propagation (Equation 5.12) [13].

$$W = \frac{1}{2}\sum \sigma : \varepsilon \qquad \text{Equation 5.11}$$

$$G = \frac{\partial U_S}{\partial C} = \frac{\partial}{\partial C}\left[U_{other} + \int W dV\right] \qquad \text{Equation 5.12}$$

Thus, with an increase in strain energy ahead of the crack, it follows that *G* also increases, as more potential energy can be released upon crack extension, making it more favorable to propagate the crack. Similarly to the calculations in Figure 4.7, the strain energy density can be tracked in grains around the crack (Figure 5.17). For comparison, the value for *W* for an isotropic, uniaxially stressed AlON sample with the averaged reported Young's modulus and Poisson's ratio [14] is calculated and displayed (Equations 5.13-15) [12].

$$\sigma = \begin{bmatrix} 0 & 0 & 0 \\ 0 & \sigma_A & 0 \\ 0 & 0 & 0 \end{bmatrix} \qquad \text{Equation 5.13}$$

$$\varepsilon = \begin{bmatrix} -\nu\sigma_A/E & 0 & 0 \\ 0 & \sigma_A/E & 0 \\ 0 & 0 & -\nu\sigma_A/E \end{bmatrix} \qquad \text{Equation 5.14}$$

$$W = \frac{1}{2}\sum \sigma : \varepsilon = \frac{\sigma_A^2}{2E} = \frac{F^2}{2EA^2} \qquad \text{Equation 5.15}$$

$F$ = force on sample $A$ = area of sample face contacting the compression platens

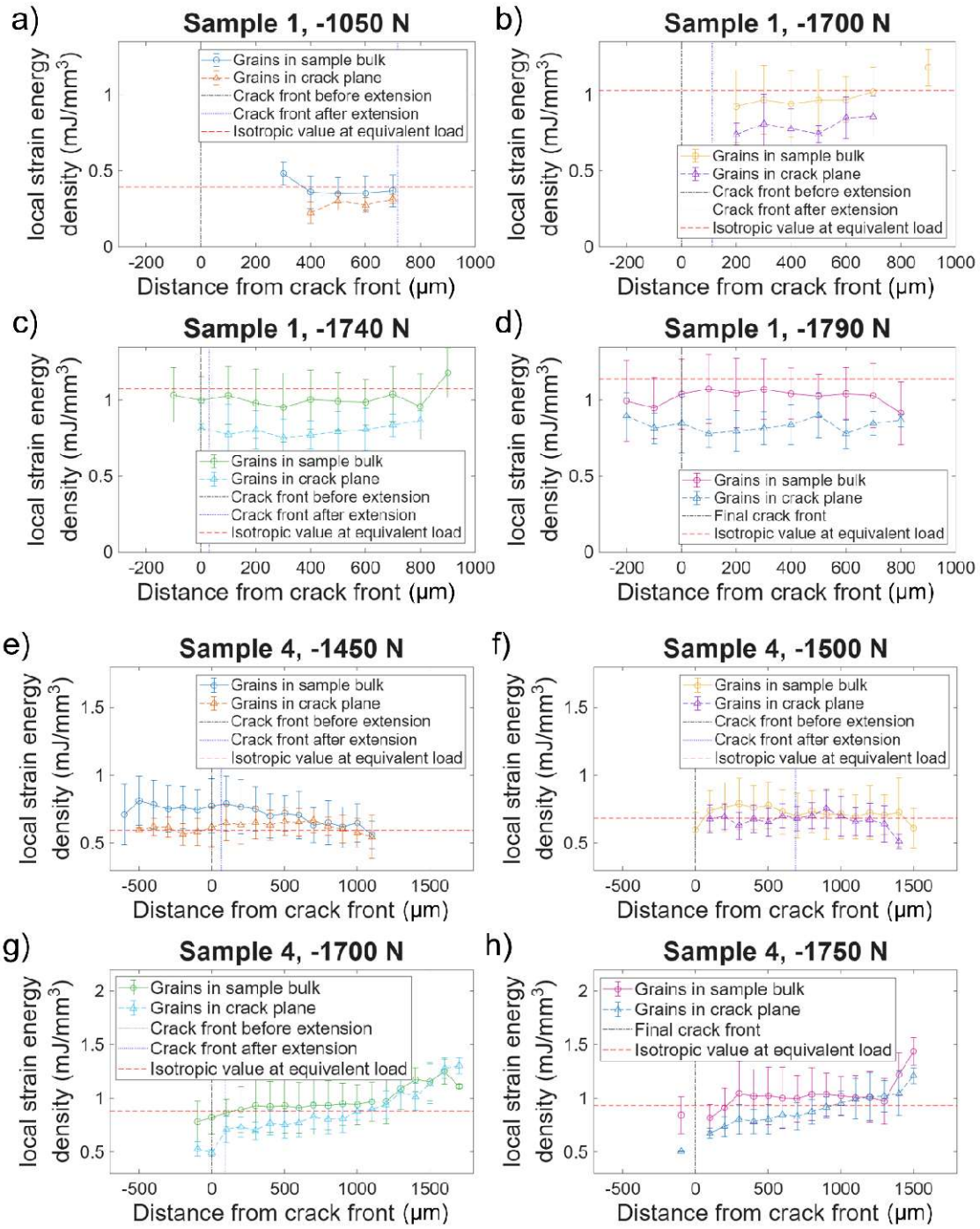


Figure 5.17: Strain energy density as a function of distance from the crack in Samples 1 and 4, compared to the expected value for an isotropic sample at equivalent load. a-d) Sample 1. e-h) Sample 4.

The gradient in $\sigma_{yy}$ with distance from the crack tip noted in Chapter 4.4.1 directly affects the strain energy density, with a similar, positive gradient present in Sample 4 ahead of the crack at -1700 N and -1750 N (Figure 5.17g-h), where the initial crack and the secondary branching crack stopped growing, respectively. While these volumes did not crack over the duration of the experiment, they were accumulating strain energy as the stress continued to build without any extension to relieve it locally. In fact, for most of the volumes studied, the data for which was collected immediately after extension, the strain energy density remained mostly flat or decreased ahead of the crack front, indicating little additional impetus for the crack to extend.

Interestingly, the positive gradient in $W$ for Sample 4 at the crack's final extensions is more prominently present far from the crack front, with the local volume just ahead of the crack still somewhat depressed, especially for the volume at lower load, and therefore lower stress.

The region just ahead of the crack front still shows an increasing trend, but the internal stress was not relieved by crack extension even after bringing the sample up in load to -1900 N. Investigation into that volume might reveal why no crack extension occurred despite the stress conditions being apparently favorable.

With the tessellations, the grain volumes can be considered at smaller sub-volumes than the 100-μm tall FF-HEDM volumes, and thus more localized effects can be considered. Specifically, when considering the average orientation of the grains with which the crack interacts, such information can be extracted for small sub-volumes such as those the crack extended through during its localized bursts of movement. Figure 5.18 shows the volume-averaged orientations, using the tessellated volumes as a basis, of the regions ahead of the crack, overlaid with the average length of the crack extensions seen in Figure 4.8. From the top of the tessellation to about 1500 μm, around which length the crack grew in short events and eventually stopped growing over a 200 N increase in load, the average plane orientation perpendicular to the crack was closest to the <110> directions. For the next few hundred microns of depth, that average normal moved closer to <111> directions before further changing to close to the <100> orientations. When the crack did eventually extend, in the nearly 800 μm fourth extension event, and in the subsequent branch pop-in and extension, it

moved fully past the near-<100> region before again stopping in a region closest to the <111> normals, with another near-<100> region existing ahead.

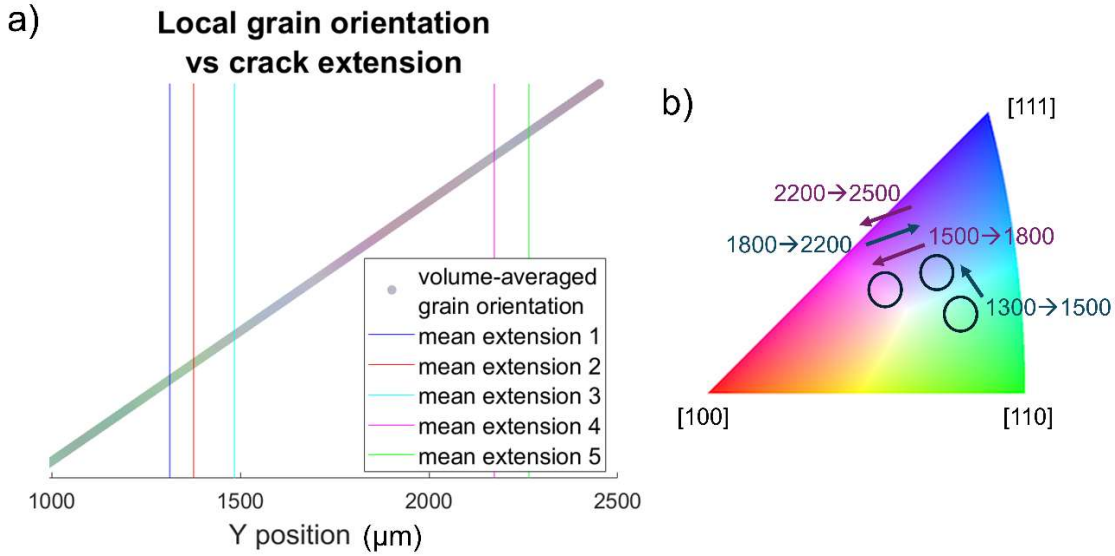


Figure 5.18: a) Crack extension in Sample 4 plotted against volume-averaged grain orientation, colored by standard IPF colors, for 2D slices in *y*. b) Standard IPF colors by orientation, with the average orientations for regions in a) marked and labeled, showing the transition between regions as a function of sample depth.

While, again, the crack does not show any major preferences for its eventual orientation within a grain, nor are individual grains of specific orientation more prone to arresting its motion, this result does suggest that when considering larger volumes and groups of grains, the total effect of grain orientation and the future crack plane orientation can serve to prevent crack extension and affect fracture toughness. Notably, in FCC materials, including AlON, the {111} planes are considered more prone to slippage and cracking [11], so the fact that the volumes ahead of the crack's stopped locations have a larger portion of <111>-oriented grains, perpendicular to the {111} planes, might play a role in why more energy must be accumulated to crack those regions. Once enough load has been achieved, the crack then moves fully past those regions before stopping at a similar localized group of orientations. This effect can be related to that hypothesized in Chapter 4.4.1, where regions of higher fracture toughness arrest the crack, and subsequent long extensions indicate it moving through a region with lower fracture toughness than that just experienced. Thus, a further

hypothesis can be created, that groups of grains of related orientations can create these regions of varying toughness.

### *5.4.2 Grain boundary and trijunction effects on crack orientation*

Beyond the orientations of grains, the orientation of grain boundaries can also be explored using tessellations and the access they provide into sub-volumes of FF-HEDM data. As in the previous section, groups of grains and local changes can be examined to glean more information beyond the average orientations of grains which interacted with the crack in different ways.

One hypothesis that can be explored from the previous chapter is whether a grain boundary's proximity to the crack is a major factor in whether the crack will move intergranularly. Additional questions can be posited about the angle of the grain boundary compared to that of the crack, the misorientation of the two grains on either side of the grain boundary, and the amount by which the crack moves to intersect such a boundary at distances far from it. Some of these questions will be considered, with Figure 5.19 assisting the explanations.

In Figure 5.19a, the effect of grain boundary orientation in the sample is related to that of the crack. In general, the more angled the boundary is to the centerline of the sample, the greater the deviation the crack must make (when compared to its average linear profile) to intercept it; at the same time, grain misorientation shows little effect on that deflection (Figure 5.19b). Therefore, nearby grain boundaries of the correct orientation are more likely to be intergranular than those angled more dramatically to the crack, lending additional credence to the observation in Chapter 4.4.3, that intergranular fracture generally occurs as a result of grain boundary proximity and similarity to the existing crack.

When considering the initial deflection to the final orientation when leaving the grain boundary (compared to the crack's average linear profile over 300 μm at depths 50 μm above and below the boundary), the crack is found to generally have a smaller deflection upon exiting than it did upon entering (Figure 5.19c). Two possibilities therefore arise: that the crack has a persistent orientation shift as a result of the boundary, or that the boundary was closer to the crack's orientation deeper in the sample, and affected it enough to divert it even when a larger deflection would be required. These effects are difficult to uncouple, especially when other nearby grains are also affecting the crack's local orientation. However, the second

possibility may serve to explain the instances with particularly large deviations which are diminished upon the crack's exit from the boundary.

A final question arises due to Sample 4's more angled profile to the centerline of the sample when compared to Sample 1, even before the branching (Figure 4.3): whether the grain boundary deflections serve to orient the crack closer to straight through the sample center. However, when comparing the crack's deviation not from its linear profile but from the centerline of the sample before and after grain boundary interception, the crack is not found to substantially be diverted toward a more centered profile and instead retains a similar overall angle to the centerline (Figure 5.19d). Thus, grain boundaries may affect the crack locally but, as Figure 5.19a shows, the closeness to the angle the crack makes with the boundary is more of an effect than any possible future angular change the crack might make toward growing straight in the center.

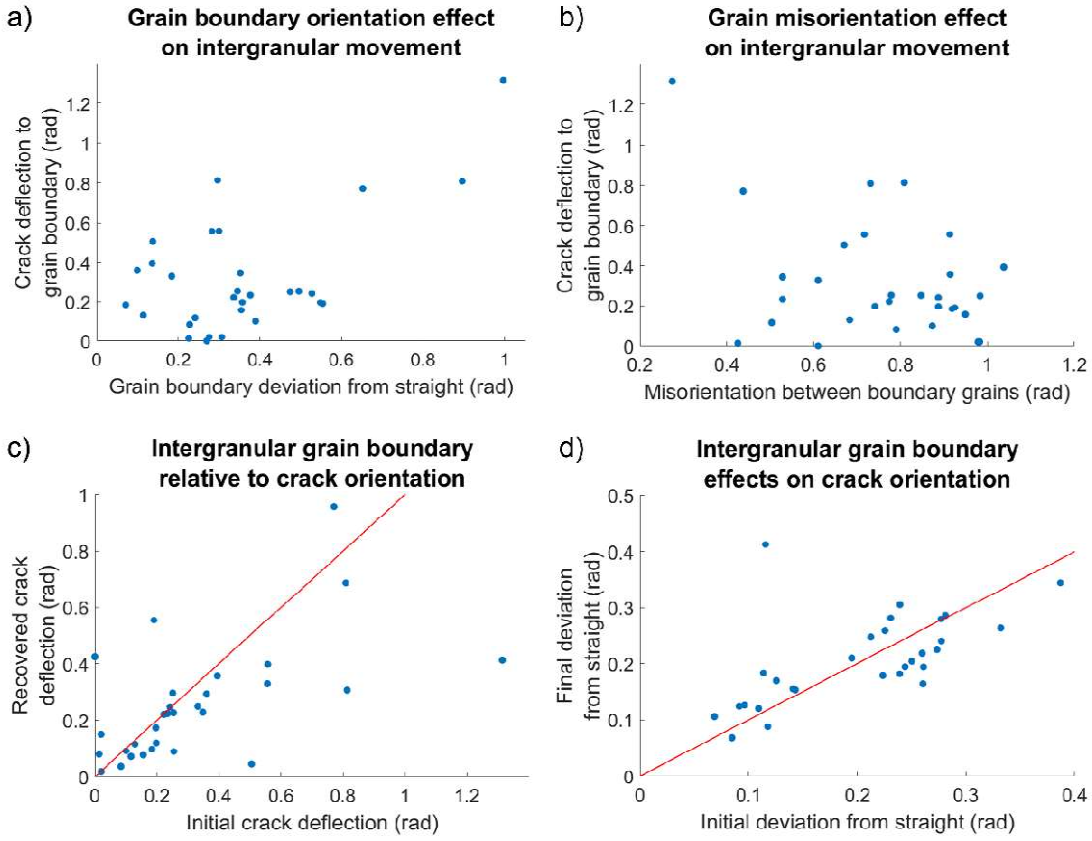


Figure 5.19: Intergranular grain boundary properties. a) The greater the angle the grain boundary makes to the centerline of the sample, the more the crack has to deflect to intercept it. b) The misorientation of the grains on either side of an intergranular grain boundary do not determine the crack's deflection. c) In general, the crack's initial deflection to intercept a grain boundary is greater than the angle it makes to the grain boundary after leaving. d) The angle the crack makes to the centerline of the sample does not change dramatically before and after following an intergranular grain boundary.

Some of these grain boundary effects are presented in more detail within the tessellated volumes in Figures 5.20 and 5.21. Figure 5.20 shows several 2D slices in the region cracked by the first crack extension, located roughly 50 μm apart in depth, and points out interactions with a few grains. In Figure 5.20a, the crack has intersected (to within one voxel) two trijunctions, pointed out in white arrows. Additionally, a short intergranular section is observed emanating out of the trijunction labeled in the lower half of the image (maroon arrow). 50 μm deeper, in Figure 5.20b, the crack is still near both trijunctions in the upper

portion. While it has moved away from the previously intergranularly-cracked boundary in the lower half, a small kink still remains in the crack's profile, roughly parallel to that boundary (gray arrow). In the upper half of the image, after leaving the trijunction, the crack has not substantially changed its angle, but now follows a grain boundary for nearly its entire length between two grains. Another 50 μm deeper, in Figure 5.20c, that intergranular section has disappeared, but again without much angular change, the crack now intersects a trijunction on the other side of the region the intergranular crack traversed. Essentially, the crack mostly followed a straight path between two trijunctions not connected by the same two grains, and in the process intersected with a grain boundary. In Figure 5.20d, the lower portion of the crack once more has a short intergranular section coincident on the same grain boundary as before, again tied to a trijunction, although a different one. Just as the kink from the first grain boundary intersection remained present for more than 100 μm, comparing this new intergranular section to the previous images shows that another kink had already developed 150 μm higher in the sample and slowly grew closer to the grain boundary until it became an intergranular section.

Fully determining how persistent these kinks are above and below the intergranular or intersection points, and therefore the force of attraction between the crack and the boundaries, is complicated due to the presence of other grains and grain boundaries. However, what is demonstrated is that even if a grain ultimately cracks transgranularly, its grain boundaries may serve as attractive regions for the crack to move through for short intervals during propagation. The grains identified as fully being intergranular (Figures 4.9-10, 5.12-13) may simply be those with a short boundary parallel to the crack which diverges above and below the point of contact; thus, their difference in orientation distribution from the transgranular grains, which may contain intergranular sections but which have boundary extrema farther from the crack, is unsurprising. Additionally, the presence of trijunctions on either side of a grain boundary may serve to direct the crack along such local grain boundaries.

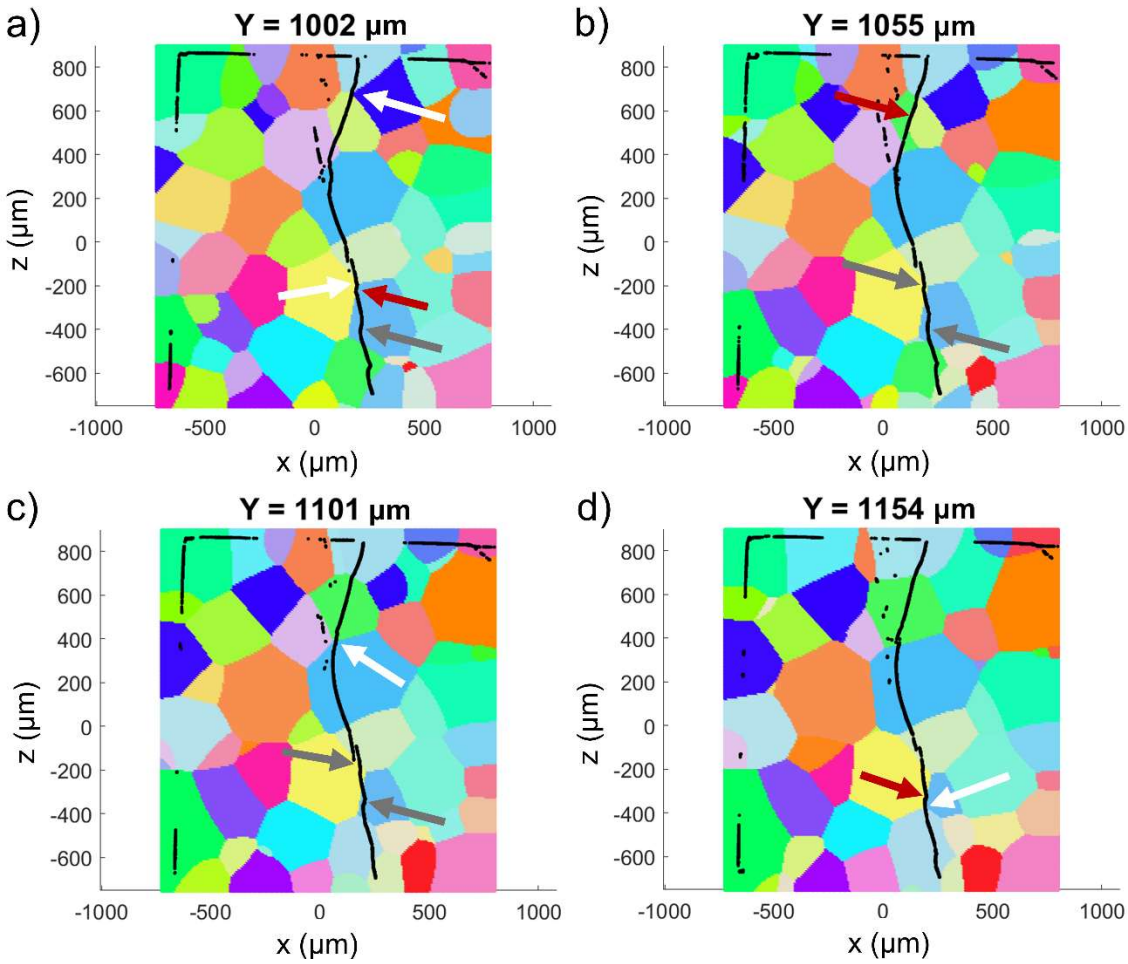


Figure 5.20: 2D slices of the tessellation for Volume 1 of Sample 4, overlaid with the final crack profile (black). White arrows mark the crack's intersection with a trijunction, maroon arrows indicate where the crack follows a grain boundary, and gray arrows point out kinks in the crack profile before and after one of the previous intersection types. a) The crack intersects with one trijunction near the top and one near the bottom, with the latter intersection extending into a local grain boundary for intergranular cracking. b) The crack leaves the upper trijunction and follows a parallel grain boundary; the crack also leaves the lower trijunction and boundary but retains a kink parallel to the grain boundary. c) The upper portion of the crack intersects with another trijunction. d) The lower portion of the crack has another section run parallel to the same grain boundary as in a), but pinned at the opposite trijunction.

In another region, this one within the near-[111] region pointed out in Figure 5.18, some of the extent of granular interaction effects on the crack can be seen. More intergranular

sections and trijunction intersections are present in this section than the previous, potentially because of the region's resistance to cracking. Some of the grain boundaries might have served as easier-to-crack sections for the crack experiencing a paucity of low-energy locations through which to move. Specifically, the crack stays pinned at some of these regions, even when the crack must deflect to do so as boundaries and trijunctions move out of the crack's path. For instance, in the purple grain in the lower portion of Figure 20b-d, located about 75 μm apart in depth, the crack cuts transgranularly through it while intersecting with two opposing trijunctions. Even before the grain appears in the slice (Figure 20a), the crack has developed a curve in the region where the grain is about to appear as if to intercept the trijunction upon its genesis. Then, when the trijunction is about to move away from the crack, it again develops a curve following the trijunction's direction of movement, potentially indicating some favorability for staying pinned rather than continuing along a straight path. Additionally, upon its exit from both trijunctions in the grain, the crack cleaves through or parallel to grain boundaries on either side, following them intergranularly for a time before diverging. In the upper portion of the images, another series of intersected trijunctions and intergranular cracks is visible, with several smaller grains overtaking each other one-by-one and allowing the intersections to persist, all without the crack's orientation changing substantially.

Fully understanding the energy landscape in these regions remains complicated, although phase-field models show promise for uniting many aspects of the complex continuum mechanics present among these collections of grains [15–17]. The crack does clearly respond to changes resulting from the way grains of different sizes and orientations are arranged, so accurately capturing the variation in stress between and within grains via models will be a major step forward in understanding how and where cracks propagate in polycrystals.

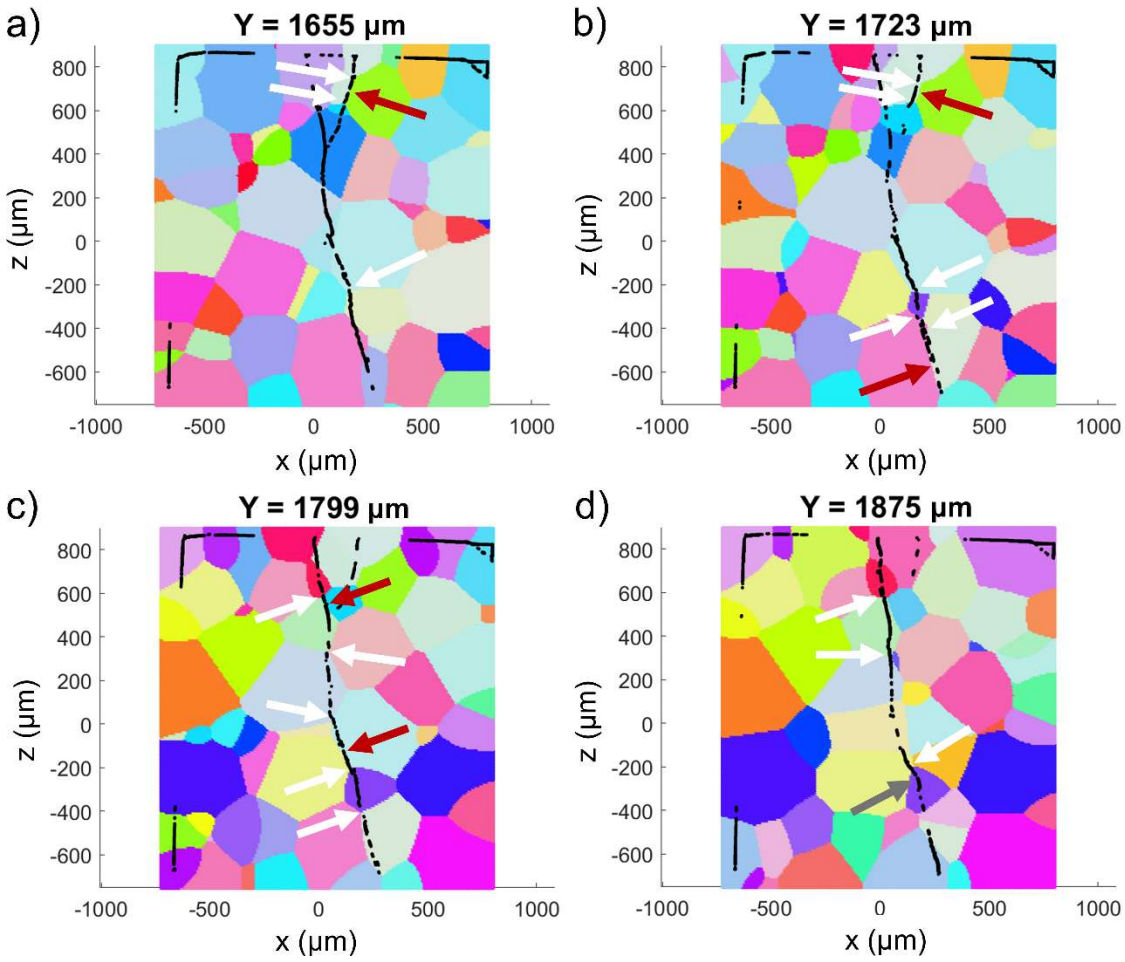


Figure 5.21: 2D slices of the tessellation for Volume 1 of Sample 4, overlaid with the final crack profile (black). White arrows mark the crack's intersection with a trijunction, maroon arrows indicate where the crack follows a grain boundary, and gray arrows point out kinks in the crack profile before and after one of the previous intersection types. a) The upper portion of the crack follows a grain boundary and intersects with both of the bordering trijunctions. b) The crack remains at the upper grain boundary; the lower portion of the crack bisects a grain through two trijunctions. c) A branch of the upper portion of the crack coincides with a trijunction and grain boundary; the lower portion remains pinned at the same trijunctions and also extends near grain boundaries on either side. d) The upper branch remains at the same trijunction; the lower portion does as well but has to develop a kink to stay pinned.

## 5.5 Conclusion

FF-HEDM data from AlON has been shown to produce maps of grains and microstructure with good agreement to more precise but more costly NF-HEDM data. As a result, conclusions about characteristics of grains which interacted with the crack in different ways can be expanded, and additional information about grains which arrested the crack gained. Exploring the latter reveals trends in the orientation of grain boundaries opposing the crack's motion, with those arresting the crack for longest being close to perpendicular to the crack's direction of propagation. Furthermore, arresting grains demonstrate a slight response toward accumulating stress in the crack opening direction with further application of load, as the energy required to overcome the resistance to cracking increases there.

Additionally, information on the average orientation of grains ahead of the crack is presented. With smaller volumetric subdivisions available from the tessellation than from the full FF-HEDM scans, gradual changes in the orientations of the collected grains are revealed, with many more grains with {111} planes perpendicular to the crack present ahead of regions where it stopped moving, as compared to regions which did not arrest the crack. Investigation into these regions shows that the crack interacted with more grain boundaries and trijunctions in the apparently unfavorable regions than in regions with more {110} planes perpendicular to the crack's direction of propagation.

Taken together with the results from full NF-HEDM, the promise of synchrotron experiments for capturing in-situ cracks in brittle materials with heterogeneous and anisotropic microstructure is extended further. The combination of HEDM and CT allows for both small-scale and larger-scale microstructural analyses around a growing crack, all of which is useful for obtaining data on specific grains as well as how the properties of those grains affect each other to allow or hinder crack propagation. While individual grains do not display obvious trends which would mark them as being predestined to crack in a certain way, the larger surrounding volume and nearby grains play a crucial role in determine the crack's motion through, around, or abutting against specific grains. As the stresses and strains within the material vary within and between grains, affected by their size, orientation, and boundary location, so too do the forces on the crack change, resulting in angular deviations and arrests that cannot be associated with any one grain or even a few local grains.

The use of phase-field models should hopefully prove promising in addressing such field inhomogeneities and their emergent effects on the crack's path and loading response,

especially for modeling the relationship between how grains distribute stress among themselves and where the crack eventually moves. However, volumetric considerations must be considered, as increasing the size of a studied volume to capture all intergranular effects increases computation costs. Performing experiments on other materials may help reveal what effect grain size, sample size, and material choice have on the internal length and other properties used to determine how material properties change throughout the field, so that the necessary information most impacting the crack's progression can be prioritized.

**Bibliography**

[1] V. Tari, R.A. Lebensohn, R. Pokharel, T.J. Turner, P.A. Shade, J.V. Bernier, A.D. Rollett, Validation of micro-mechanical FFT-based simulations using high energy diffraction microscopy on Ti-7Al, *Acta Mater* 154 (2018) 273–283. https://doi.org/10.1016/j.actamat.2018.05.036.
[2] S. Falco, J. Jiang, F. De Cola, N. Petrinic, Generation of 3D polycrystalline microstructures with a conditioned Laguerre-Voronoi tessellation technique, *Comp Mater Sci* 136 (2017) 20–28. https://doi.org/10.1016/j.commatsci.2017.04.018.
[3] J. Kim, Y. Hayashi, S.S. Ha, M. Yabashi, Tessellation-based grain boundary determination for X-ray orientation microscopies, *Comput Phys Commun* 320 (2026) 109988. https://doi.org/10.1016/j.cpc.2025.109988.
[4] W.A. Tayon, D.C. Pagan, S.R. Yeratapally, T.Q. Phan, J.D. Hochhalter, Exploring the role of Type-II residual stresses in a laser powder bed fusion nickel-based superalloy using measurement and modeling, *Int J Fatigue* 181 (2024) 108153. https://doi.org/10.1016/j.ijfatigue.2024.108153.
[5] Q. Du, V. Faber, M. Gunzburger, Centroidal Voronoi tessellations: applications and algorithms, *SIAM Rev* 41 (1999) 637–676. https://doi.org/10.1137/S0036144599352836.
[6] B. Chen, D. Li, P. Davies, R. Johnston, X. Ge, C. Li, Recent progress of digital reconstruction in polycrystalline materials, *Arch Computat Methods Eng* 32 (2025) 3447–3498. https://doi.org/10.1007/s11831-025-10245-4.
[7] D. Wolf, Correlation between energy, surface tension and structure of free surfaces in fcc metals, *Surf Sci* 226 (1990) 389–406. https://doi.org/10.1016/0039-6028(90)90502-Y.
[8] R. Tran, Z. Xu, B. Radhakrishnan, D. Winston, W. Sun, K.A. Persson, S.P. Ong, Surface energies of elemental crystals, *Sci Data* 3 (2016) 160080. https://doi.org/10.1038/sdata.2016.80.
[9] B. Fu, W. Liu, Z. Li, Calculation of the surface energy of fcc-metals with the empirical electron surface model, *Appl Surf Sci* 256 (2010) 6899–6907. https://doi.org/10.1016/j.apsusc.2010.04.108.
[10] J. Wang, S.-Q. Wang, Surface energy and work function of fcc and bcc crystals: Density functional study, *Surf Sci* 630 (2014) 216–224. https://doi.org/10.1016/j.susc.2014.08.017.
[11] J.J. Guo, K. Wang, T. Fujita, J.W. McCauley, J.P. Singh, M.W. Chen, Nanoindentation characterization of deformation and failure of aluminum oxynitride, *Acta Mater* 59 (2011) 1671–1679. https://doi.org/10.1016/j.actamat.2010.11.034.
[12] Constitutive Equations, in: An Introduction to Continuum Mechanics with Applications, Cambridge University Press, n.d.: pp. 178–209.
[13] Linear fracture mechanics, in: Fracture Mechanics with an Introduction to Micromechanics, Springer, 2006: pp. 49–57. https://doi.org/10.1007/b22134.
[14] S. Satapathy, M. Ahart, D. Dandekar, R.J. Hemley, B. Schuster, P. Khoma, Single-Crystal Elastic Properties of Aluminum Oxynitride (AlON) from Brillouin Scattering, *J Amer Ceram Soc* 99 (2016) 1383–1389. https://doi.org/10.1111/jace.14065.
[15] R. Kiran, K. Choudhary, N. Nguyen-Thanh, Phase-field modeling of brittle anisotropic fracture in polycrystalline materials under combined thermo-mechanical loadings, *Comput Struct* 308 (2025) 107651. https://doi.org/10.1016/j.compstruc.2025.107651.

[16] S. Riad, D. Bardel, J. Réthoré, Unified phase field model to simulate both intergranular and transgranular failure in polycrystalline aggregates, *Finite Elem Anal Des* 194 (2021) 103555. https://doi.org/10.1016/j.finel.2021.103555.
[17] J.D. Clayton, J. Knap, Phase field modeling of directional fracture in anisotropic polycrystals, *Comp Mater Sci* 98 (2015) 158–169. https://doi.org/10.1016/j.commatsci.2014.11.009.